



Buckling Design and Analysis of a Payload Fairing 1/6th Cylindrical Arc-Segment Panel

Daniel N. Kosareo
Vantage Partners LLC, Brook Park, Ohio

Stanley T. Oliver
Marshall Space Flight Center, Huntsville, Alabama

Brett A. Bednarcyk
Glenn Research Center, Cleveland, Ohio

NASA STI Program . . . in Profile

Since its founding, NASA has been dedicated to the advancement of aeronautics and space science. The NASA Scientific and Technical Information (STI) program plays a key part in helping NASA maintain this important role.

The NASA STI Program operates under the auspices of the Agency Chief Information Officer. It collects, organizes, provides for archiving, and disseminates NASA's STI. The NASA STI program provides access to the NASA Aeronautics and Space Database and its public interface, the NASA Technical Reports Server, thus providing one of the largest collections of aeronautical and space science STI in the world. Results are published in both non-NASA channels and by NASA in the NASA STI Report Series, which includes the following report types:

- **TECHNICAL PUBLICATION.** Reports of completed research or a major significant phase of research that present the results of NASA programs and include extensive data or theoretical analysis. Includes compilations of significant scientific and technical data and information deemed to be of continuing reference value. NASA counterpart of peer-reviewed formal professional papers but has less stringent limitations on manuscript length and extent of graphic presentations.
- **TECHNICAL MEMORANDUM.** Scientific and technical findings that are preliminary or of specialized interest, e.g., quick release reports, working papers, and bibliographies that contain minimal annotation. Does not contain extensive analysis.
- **CONTRACTOR REPORT.** Scientific and technical findings by NASA-sponsored contractors and grantees.

- **CONFERENCE PUBLICATION.** Collected papers from scientific and technical conferences, symposia, seminars, or other meetings sponsored or cosponsored by NASA.
- **SPECIAL PUBLICATION.** Scientific, technical, or historical information from NASA programs, projects, and missions, often concerned with subjects having substantial public interest.
- **TECHNICAL TRANSLATION.** English-language translations of foreign scientific and technical material pertinent to NASA's mission.

Specialized services also include creating custom thesauri, building customized databases, organizing and publishing research results.

For more information about the NASA STI program, see the following:

- Access the NASA STI program home page at <http://www.sti.nasa.gov>
- E-mail your question to help@sti.nasa.gov
- Fax your question to the NASA STI Information Desk at 443-757-5803
- Phone the NASA STI Information Desk at 443-757-5802
- Write to:
STI Information Desk
NASA Center for AeroSpace Information
7115 Standard Drive
Hanover, MD 21076-1320



Buckling Design and Analysis of a Payload Fairing 1/6th Cylindrical Arc-Segment Panel

Daniel N. Kosareo
Vantage Partners LLC, Brook Park, Ohio

Stanley T. Oliver
Marshall Space Flight Center, Huntsville, Alabama

Brett A. Bednarcyk
Glenn Research Center, Cleveland, Ohio

National Aeronautics and
Space Administration

Glenn Research Center
Cleveland, Ohio 44135

Trade names and trademarks are used in this report for identification only. Their usage does not constitute an official endorsement, either expressed or implied, by the National Aeronautics and Space Administration.

Level of Review: This material has been technically reviewed by technical management.

Available from

NASA Center for Aerospace Information
7115 Standard Drive
Hanover, MD 21076-1320

National Technical Information Service
5301 Shawnee Road
Alexandria, VA 22312

Available electronically at <http://www.sti.nasa.gov>

Buckling Design and Analysis of a Payload Fairing 1/6th Cylindrical Arc-Segment Panel

Daniel N. Kosareo
Vantage Partners LLC
Brook Park, Ohio 44142

Stanley T. Oliver
National Aeronautics and Space Administration
Marshall Space Flight Center
Huntsville, Alabama 35812

Brett A. Bednarczyk
National Aeronautics and Space Administration
Glenn Research Center
Cleveland, Ohio 44135

Abstract

Design and analysis results are reported for a panel that is a 1/6th arc-segment of a full 33-ft diameter cylindrical barrel section of a payload fairing structure. Six such panels could be used to construct the fairing barrel, and, as such, compression buckling testing of a 1/6th arc-segment panel would serve as a validation test of the buckling analyses used to design the fairing panels. In this report, linear and nonlinear buckling analyses have been performed using finite element software for 1/6th arc-segment panels composed of aluminum honeycomb core with graphite/epoxy composite facesheets and an alternative fiber reinforced foam (FRF) composite sandwich design. The cross sections of both concepts were sized to represent realistic Space Launch Systems (SLS) Payload Fairing panels. Based on shell-based linear buckling analyses, smaller, more manageable buckling test panel dimensions were determined such that the panel would still be expected to buckle with a circumferential (as opposed to column-like) mode with significant separation between the first and second buckling modes. More detailed nonlinear buckling analyses were then conducted for honeycomb panels of various sizes using both Abaqus and ANSYS finite element codes, and for the smaller size panel, a solid-based finite element analysis was conducted. Finally, for the smaller size FRF panel, nonlinear buckling analysis was performed wherein geometric imperfections measured from an actual manufactured FRF were included. It was found that the measured imperfection did not significantly affect the panel's predicted buckling response.

1.0 Introduction

The Advanced Exploration Systems (AES), Composite for Exploration (CoEx) payload fairing project was tasked to design a composite honeycomb sandwich construction for use in the Space Launch Systems (SLS) Payload Fairing. The CoEx payload fairing project is a follow-on of the Lightweight Spacecraft Structures and Materials (LSSM) project, and its predecessor, the Structural Concepts Element of the Advanced Composites Technology (ACT) project. The goal of these three projects was to advance the Technology Readiness Level (TRL) of large scale composite structures for heavy lift launch vehicles. The CoEx Payload Fairing project was focused on a honeycomb sandwich construction for its maturity, affordability, and performance capability to support the SLS Payload Fairing design. This report also discusses the design and analysis of an alternate 1/6th Fiber Reinforced Foam (FRF) (Bednarczyk et al., 2010, 2011; Zalewski and Bednarczyk, 2010) panel design, whose main purpose was to serve as a pathfinder for the honeycomb sandwich panel manufacturing and testing. This was referred to as the Tool Try Panel (TTP) for the first manufacturing demonstration of the new 1/6th tool.

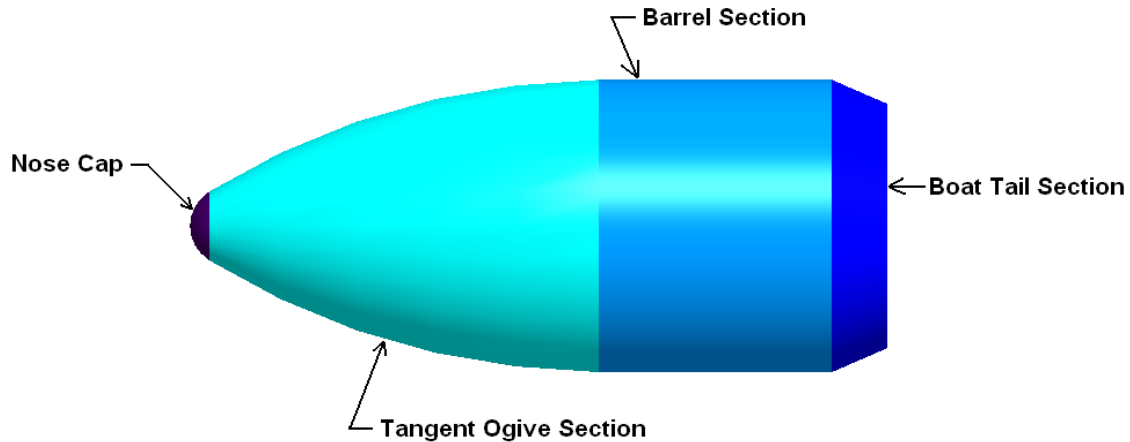


Figure 1.—CoEx payload fairing configuration, PF2-COEX-28.

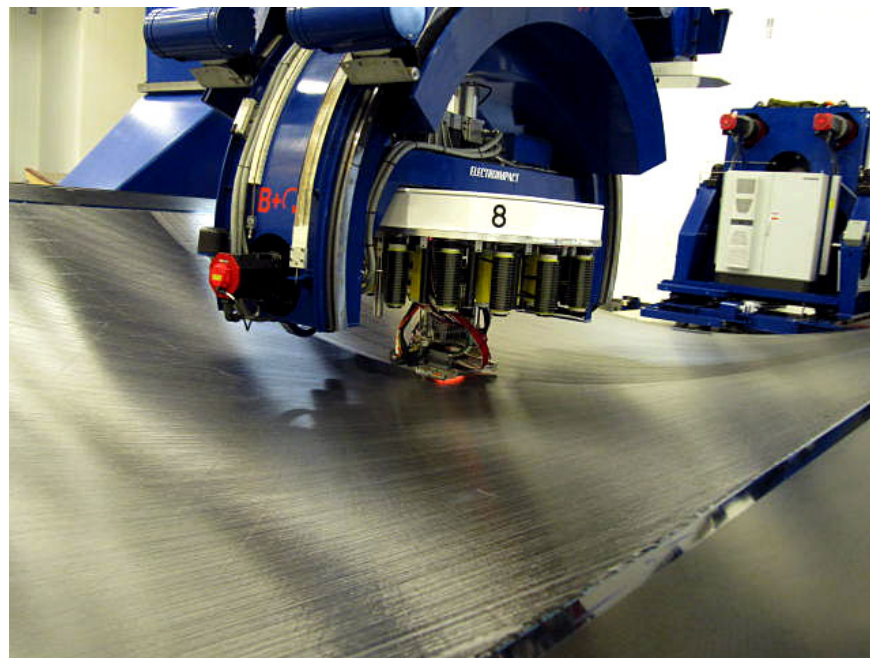


Figure 2.—Fiber placement at Spirit Aerosystems.

This paper documents the design of the 1/6th arc segment panel, which represents a segment of the barrel (or cylindrical) section of the payload fairing as shown in Figure 1. Although the SLS Payload Fairing Block 1A baseline design has an 8.4-m (27.6-ft) diameter, a 10-m (33-ft) diameter payload fairing design, the SLS Block 2 configuration was chosen to maintain continuity with, and to build upon, previous work performed in the LSSM and ACT projects. The goal was to design and build an arc-segment buckling test panel that mimicked the structural behavior of a full cylindrical section in compression. This buckling test panel would be cut from a 27- by 18-ft (1/6th) composite sandwich panel based on a 33-ft diameter fairing built by Spirit Aerospace in Wichita, Kansas.

The 1/6th honeycomb sandwich panel was constructed of a 1-in. thick aluminum honeycomb core with 8-ply graphite/epoxy facesheets. As shown in Figure 2, Spirit Aerospace used automated fiber placement technology to produce the composite panel on NASA's panel tool and demonstrate the viability of this manufacturing process for large scale fairing structures. Figure 3 shows the overhead gantry and NASA's arc segment panel tool built by Janicki Industries on the floor.

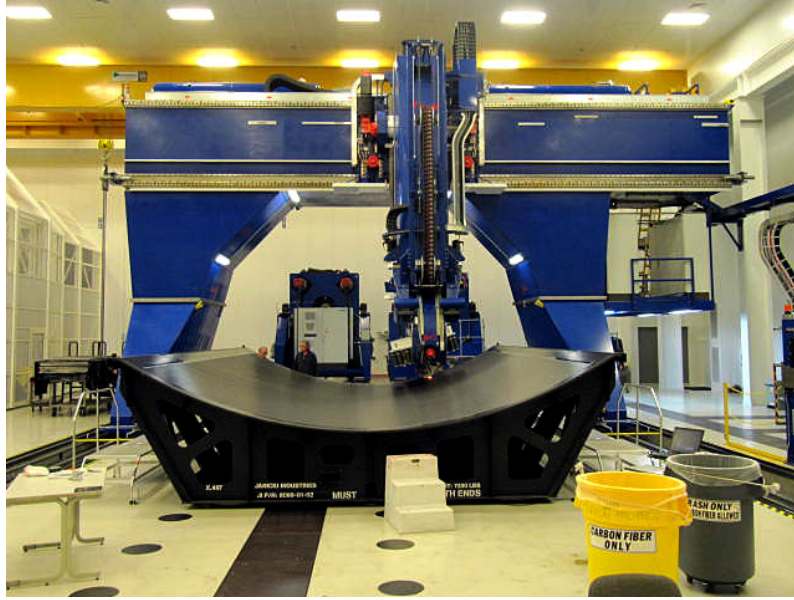


Figure 3.—Gantry and 1/6th panel tool at Spirit Aerosystems.

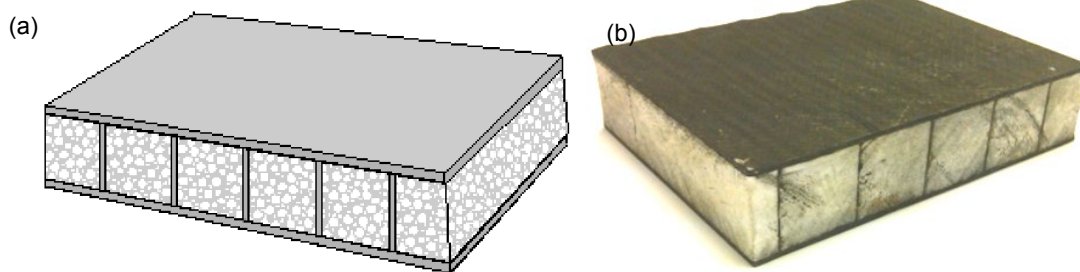


Figure 4.—Fiber reinforced foam (FRF) sandwich panel concept, (a) schematic, and (b) photograph.

The 1/6th FRF sandwich panel was constructed with a nominal total thickness of 1-in., with non-crimp fabric graphite/epoxy facesheets equivalent to 8 plies. As discussed in Bednarczyk et al., (2010, 2011) and Zalewski and Bednarczyk (2010), the FRF sandwich core consists of long rectangular cross-section sticks of foam that are wound with dry fibers (see Figure 4). These wound sticks are then assembled side-by-side, and a light polymeric scrim fabric is applied on either side to hold the sticks together and produce a continuous dry core. The core is then stacked with the hand-layed non-crimp fabric facesheets on a tool, and the entire assembly is vacuum bagged, infiltrated with epoxy resin, and oven cured. This out-of-autoclave process requires a suitable, infiltratable, epoxy resin. As shown in Figure 4, the final panel configuration includes composite webs within the core, which are formed by the infiltrated winding layers. These webs provide FRF with some additional axial extensional and bending stiffness and strength compared to foam core sandwich panels, plus a great deal of additional axial through-thickness shear stiffness and strength.

The remainder of this report describes the two composite panel types considered in the buckling analyses and then provides a detailed presentation of the buckling analyses, performed using the commercial finite element codes Abaqus and ANSYS. First, linear eigenvalue-based analyses were performed considering the full 1/6th arc segment panel dimensions, along with reduced-size panels, to determine an expedient test panel size in terms of the expected buckling mode and ease of testing. Nonlinear buckling analyses were also performed for the honeycomb sandwich configuration using both shell- and solid-based finite element models. Finally, nonlinear buckling analyses of an as-manufactured FRF panel were conducted, wherein measured imperfections were included in the analyses.

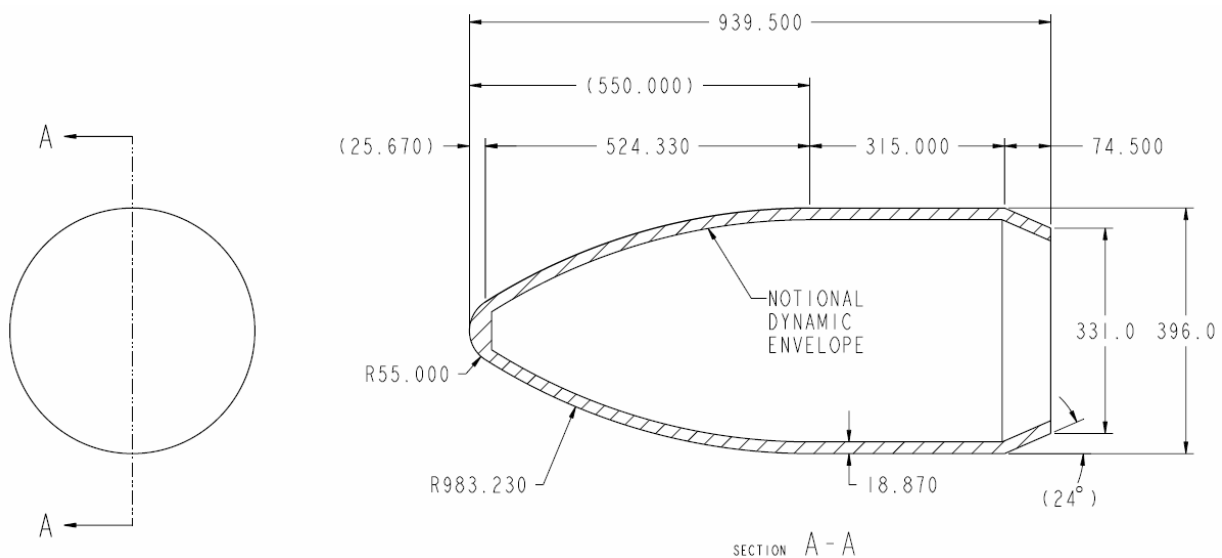


Figure 5.—CoEx payload fairing design dimensions (in inches).

2.0 Panel Layout and Material Properties

As stated earlier, the 1/6th sandwich panel designs were based on the cylindrical barrel section of the CoEx Payload Fairing configuration, with a 33-ft diameter. Referring to Figure 5, the actual dimensions of a 1/6 arc-segment of the barrel are 26.25- by 17.28-ft. The CoEx project chose 27- by 17.25-ft as the baseline panel size for the tool design, and this panel size became the initial design for analysis. This initial full 1/6th arc segment sandwich panel (27- by 17.25-ft) was investigated (along with other smaller panel sizes) using two finite element analysis (FEA) software programs, ANSYS and Abaqus.

2.1 Honeycomb Sandwich Panels

An example ANSYS 2-D layered structural shell element model of the honeycomb sandwich configuration is shown in Figure 6. An example Abaqus shell model for the honeycomb sandwich panel is shown in Figure 7. In both cases, the facesheet plies, along with the core, are modeled as layers in the layered shell elements.

As shown in Figure 6 and Figure 7, the stacking sequence of the 8-ply carbon fiber/epoxy facesheets was $[45^\circ/90^\circ/-45^\circ/0^\circ]_s$ with 0.0053 in. thick plies. The facesheet material was IM7/977-3 tape. The IM7/977-3 elastic properties allowables were obtained from the Orion Materials Database (Lockheed Martin, 2010), and they are not listed due to ITAR restrictions. Referring to Table 1, the aluminum (5052-T6 alloy) honeycomb properties were obtained from commercially available literature (Hexcel, 2013). Note that the honeycomb in-plane longitudinal and transverse moduli (E_1 and E_2) were kept at 21.28 psi, and the in-plane shear modulus (G_{12}) was kept at 5.32 psi. It is also common for these in-plane properties to be assigned an arbitrary extremely low value (c.f. Myers et al., 2013).

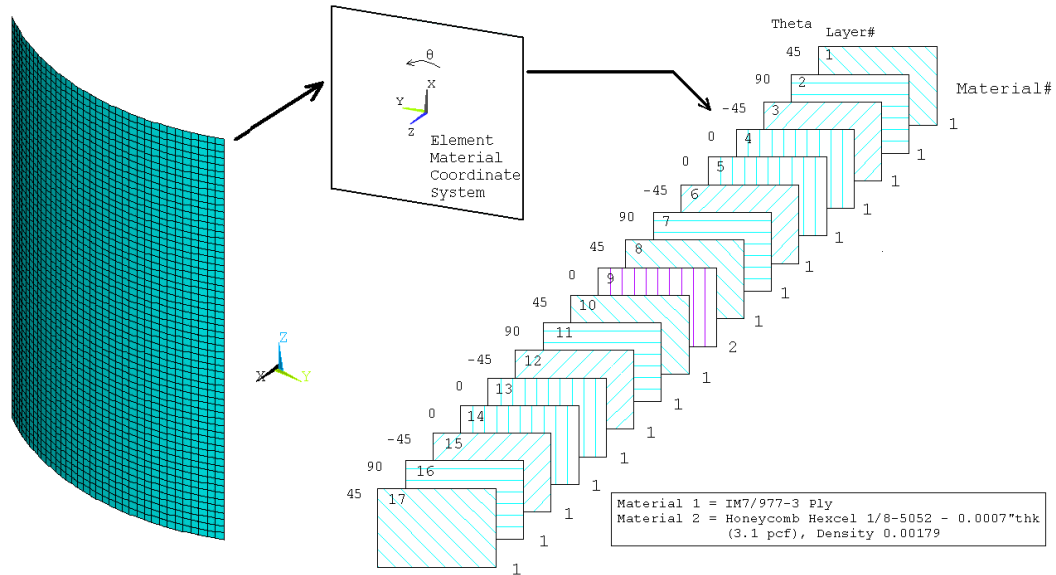


Figure 6.—ANSYS FEM of the 1/6th honeycomb sandwich panel.

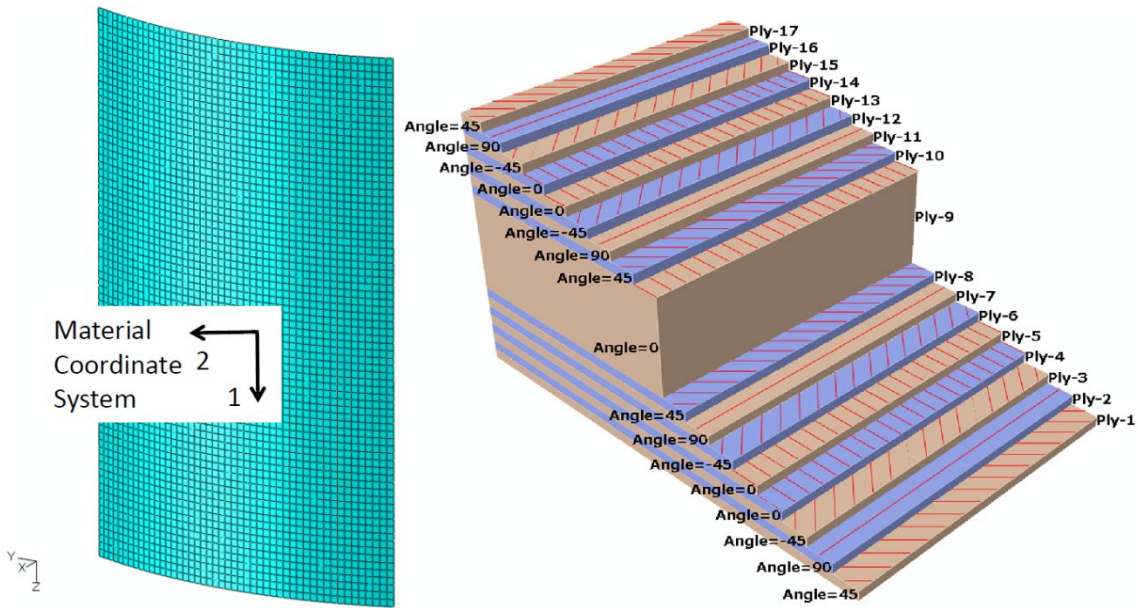


Figure 7.—Abaqus FEM of the 1/6th honeycomb sandwich panel.

TABLE 1.—ALUMINUM HONEYCOMB MATERIAL PROPERTIES,
3.1 pcf, 1/8 in.-5052-0.0007 in. THICKNESS

Property/units	Value	Property/units	Value
E_1 , psi	21.28	ρ , pcf	3.1
E_2 , psi	21.28	F_{t1} , psi	215
E_3 , ksi	75	F_{e1} , psi	215
ν_{12}	0.333	F_{t2} , psi	215
ν_{23}	1.0×10^{-5}	F_{e2} , psi	215
ν_{13}	1.0×10^{-5}	F_{t3} , psi	130
G_{12} , psi	5.32	F_{e3} , psi	300
G_{13} , ksi	45	F_{s12} , psi	90
G_{23} , ksi	22	F_{s23} , psi	90
γ , lb/in ³	0.00179	F_{s13} , psi	90

2.2 FRF Sandwich Panels

The FRF sandwich panel cross-section design considered is shown in Figure 8. This panel design was taken from the barrel section of a full FRF fairing design that considered both strength and stability failure modes. The facesheets each were designed to consist of two layers of T700 VectorPly C-QX 1800 non-crimp fabric (VectorPly, 2013), which has an internal ply stacking of $[-45^\circ/90^\circ/45^\circ/0^\circ]$ and a per ply thickness of 0.006 in. As shown in Figure 9, each sheet of the non-crimp fabric consists of unidirectional plies that are not woven together, but rather stitched with polyester fiber. Two sheets of this fabric, layed up in reverse order, form each facesheet, with an effective stacking sequence of $[-45^\circ/90^\circ/45^\circ/0^\circ]_s$. The FRF panel was designed using E862 epoxy resin. Because ply properties for this facesheet material were unavailable, they were predicted from the constituent properties (fiber/matrix) using NASA's MAC/GMC micromechanics software (Bednarczyk and Arnold, 2002), with an estimated fiber volume fraction of 60 percent. While the stiffness properties predicted by micromechanics are known to be very reliable, prediction of composite allowables using micromechanics is known to be problematic (Aboudi et al., 2013). Therefore, ply level B-Basis stress allowables for the T700/E862 facesheets were estimated based on the B-Basis strain allowables of the IM7/977-3 material used in the honeycomb sandwich panel design, with an assumed linear relation between the estimated stress allowables and assumed strain allowables. The ply level material properties for the 60 percent volume fraction T700/E862 facesheet material are given in Table 2.

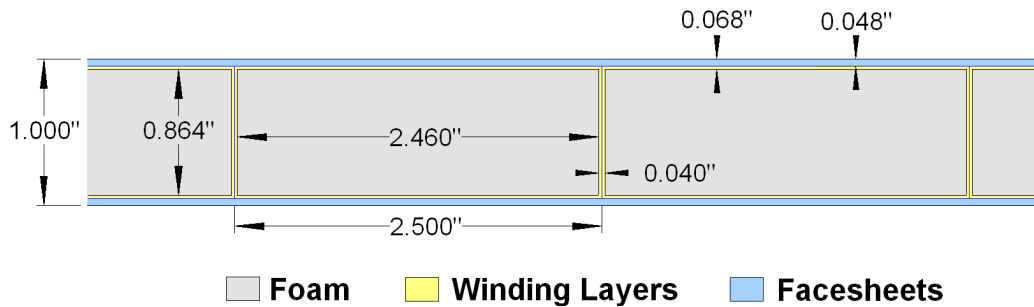


Figure 8.—FRF sandwich panel cross-section design.

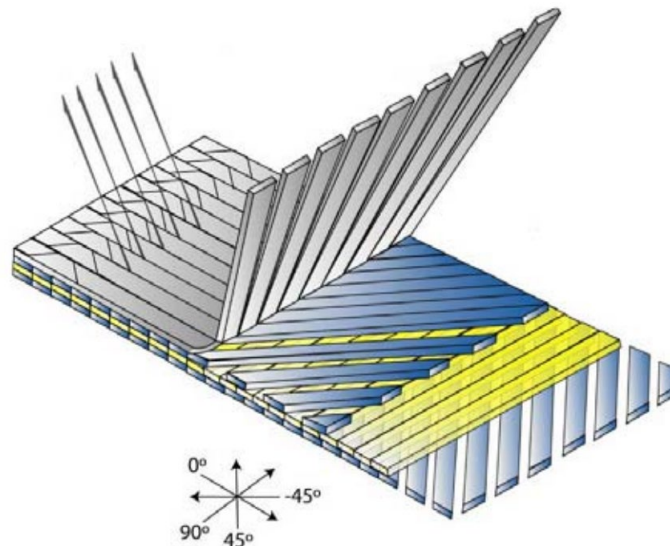


Figure 9.—Schematic of VectorPly C-QX 1800 non-crimp fabric (VectorPly, 2013).

The winding layers (see Figure 8) cannot be represented with these same material properties, even though they have the same T700/E862 constituent materials, because the fiber volume fraction that results from the winding and infiltration process is much lower. Based on an estimated fiber volume fraction of 32 percent, the winding layer ply properties were approximated using the identical process described above for the facesheet plies. These properties are given in Table 3. Note that the thickness of each winding ply was estimated to be 0.01 in., and the panel design called for two winding plies with $[+45^\circ/-45^\circ]$ layup. Thus, each web, which consists of the windings from two adjacent foam sticks, has a symmetric $[+45^\circ/-45^\circ]_s$ layup. The foam material included in the design was Rohacell 31HF polymethacrylimide foam (Evonik Industries, 2013), with material properties given in Table 4.

TABLE 2.—ESTIMATED 60 PERCENT T700/E862 PLY PROPERTIES USED IN THE FRF PANEL FACESHEET DESIGN

Property/units	Value
E_1 , Msi	20.17
E_2 , Msi	1.147
ν_{12}	0.257
G_{12} , Msi	0.465
G_{13} , Msi	0.465
G_{23} , Msi	0.330
γ , lb/in ³	0.057
Thickness, in.....	0.006
F_{t1} , ksi.....	251
F_{e1} , ksi	142
F_{t2} , ksi.....	12.5
F_{e2} , ksi	10.2
F_{s12} , psi.....	5.89

TABLE 3.—ESTIMATED 32 PERCENT T700/E862 PLY PROPERTIES USED IN THE FRF PANEL WINDING LAYER DESIGN

Property/units	Value
E_1 , Msi	10.94
E_2 , Msi	0.705
ν_{12}	0.300
G_{12} , Msi	0.237
G_{13} , Msi	0.237
G_{23} , Msi	0.207
γ , lb/in ³	0.0496
Thickness, in.....	0.01
F_{t1} , ksi.....	136
F_{e1} , ksi	77.0
F_{t2} , ksi.....	7.73
F_{e2} , ksi	6.27
F_{s12} , psi.....	3.00

TABLE 4.—ROHACELL 31HF POLYMETHACRYLIMIDE FOAM MATERIAL PROPERTIES

Property/units	Value
E , ksi.....	5.22
G , ksi.....	1.885
F_b , psi.....	145
F_c , psi.....	58
F_s , psi.....	58
γ , lb/in ³	0.001157

The complexity of the FRF sandwich panel cross-section (see Figure 4) renders it more difficult to represent using simple shell properties. As such, the commercial HyperSizer structural sizing software (Collier Research Corp., 2013) was used to generate effective extensional, coupling, and bending stiffness matrices with the software’s “Reinforced Core Sandwich (RCS)” uniaxially stiffened panel concept. These matrices, referred to a reference plane at the midpoint of the top facesheet, are,

$$\mathbf{A} = \begin{bmatrix} 943 & 368 & 0 \\ 368 & 931 & 0 \\ 0 & 0 & 385 \end{bmatrix} \times 10^3 \text{ lb/in} \quad \mathbf{B} = \begin{bmatrix} 449 & 175 & 0 \\ 175 & 443 & 0 \\ 0 & 0 & 183 \end{bmatrix} \times 10^3 \text{ in} - \text{lb/in} \quad \mathbf{D} = \begin{bmatrix} 421 & 163 & 0.5 \\ 163 & 418 & 0.5 \\ 0.5 & 0.5 & 171 \end{bmatrix} \times 10^3 \text{ in}^2 - \text{lb/in}$$

The FRF panel buckling response was evaluated using only the Abaqus finite element software.

3.0 Linear Eigenvalue Buckling Analysis

The finite element model of the panel is shown in Figure 10, along with the loading and axial boundary conditions. The lateral panel edges were left free. These identical conditions were employed, along with very similar mesh sized, for the ANSYS and Abaqus analyses of the honeycomb sandwich panel and for the Abaqus analysis of the FRF sandwich panel. Linear eigenvalue analysis was performed to predict the first buckling eigenvalue and mode shape for these models of the full size 27- by 17.25-ft panels. The results are shown in Figure 11. Clearly, the predicted first buckling mode is the same for all three cases, involving two outward radial waves at the panel edges. The ANSYS and Abaqus models of the honeycomb sandwich panel predicted eigenvalues that were very close (1.968 versus 1.972, respectively), while the Abaqus FRF sandwich panel has predicted a slightly lower eigenvalue of 1.935. This slightly lower eigenvalue can be attributed to a number of differences between the FRF and honeycomb sandwich panels, despite their identical shell dimensions. First, the FRF composite facesheet material has a lower stiffness than does the honeycomb facesheet material. Further, the FRF panel total thickness (1 in.) is lower than the honeycomb panel (1 in. core plus 16 facesheet plies that are each 0.0053 in. thick = 1.0848 in.). However, the FRF panel facesheets are thicker (0.048 in. each versus 0.0424 in.), and the FRF panel has the additional stiffness contribution of the composite winding plies. The combination of these effects resulted in the honeycomb panel having slightly higher predicted buckling resistance.

To simplify, lower cost, and provide for additional potential testing locations of the 1/6th panel, it was desirable to determine a reduced size panel that could be cut from the full size panel. This would also provide additional test specimens from the single panel. As such, the analyzed panel size was reduced, while keeping the 27 to 17.25 = 1.565 panel aspect ratio constant. It was found that, not only the predicted minimum eigenvalue of the panel changed, but also the predicted first mode changed. The Abaqus results for this panel size study for the honeycomb sandwich panel are shown in Figure 12. In this figure, the eigenvalues associated with the first four buckling modes of the full size honeycomb panel are plotted versus the panel height. For the full size panel (height = 27 ft), the first four eigenvalues are fairly close. The first mode (A), as discussed above, has an eigenvalue of 1.971 and the mode involves an axial half-wave in the same radial direction on the panel sides (edges). The second mode (B) (eigenvalue = 2.059) involves a full-wave axially in the same radial direction on the panel sides. The third mode (C) (eigenvalue = 2.140) involves a half-wave axially, but with alternating radial directions on the panel sides, and finally, the fourth mode (D) (eigenvalue = 2.311) involves a full-wave axially with alternating radial directions on the panel sides. As the panel size is reduced (while maintaining the aspect ratio), these four predicted buckling modes remain as the first four, but their order and spread changes. At a panel height of 12- to 13-ft, mode C has the lowest eigenvalue, plus a large (approximately 50 percent) difference from the next lowest eigenvalue. A large spread between eigenvalues is desirable in terms of

test versus prediction correlation because potential imperfections in the panel construction and the test set up are then less likely to cause a different actual buckling mode. Furthermore, the mode shapes with alternating radial direction on the sides are more representative of a classical periodic full cylinder buckling mode, where waves with alternating radial direction progress circumferentially around the cylinder as shown in Figure 13 (Sleight et al., 2011). For these regions, the panels with heights from approximately 10- to 14-ft were identified as a “sweet spot” for a potential test article that could be cut from the full size 1/6th honeycomb sandwich panel. This identical panel size study was repeated for the honeycomb sandwich panel using ANSYS, with nearly identical results, as shown in Figure 14. The panel size study for the FRF sandwich panel was conducted using Abaqus, with the results shown in Figure 15. The results are very similar to those of the honeycomb sandwich panel, with a clear candidate panel height of approximately 12 to 13 ft emerging as the most desirable.

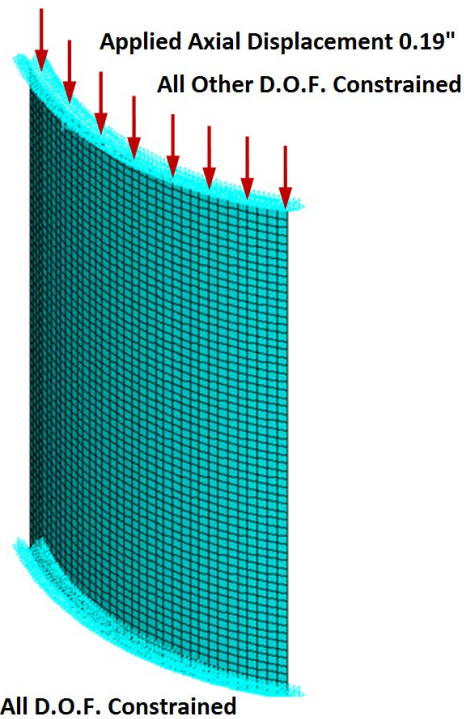


Figure 10.—Applied static load and boundary constraints on the panel finite element models.

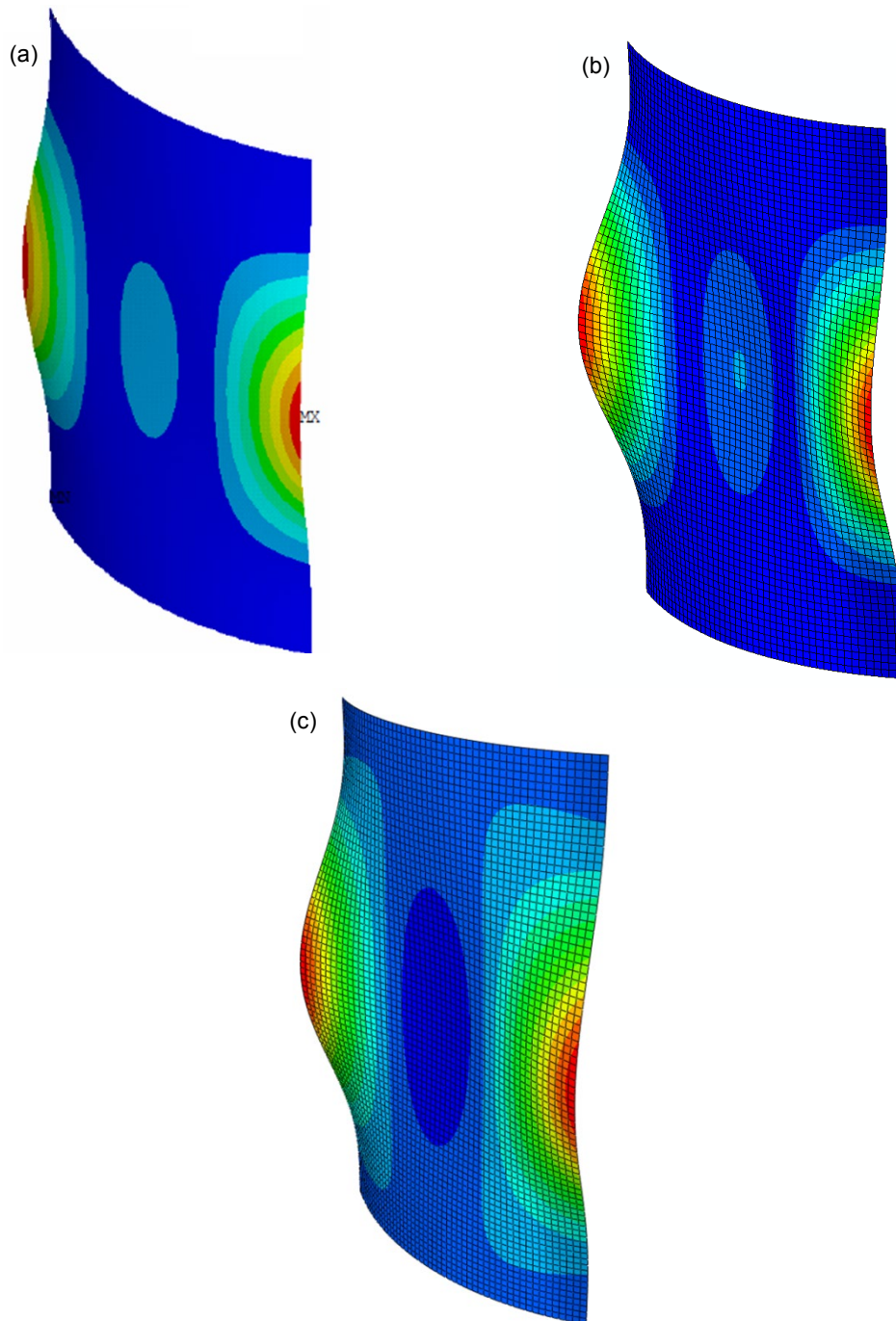


Figure 11.—First buckling mode shapes for the 27- by 17.25-ft panel. (a) Honeycomb sandwich ANSYS prediction - eigenvalue = 1.968, (b) Honeycomb sandwich Abaqus prediction - eigenvalue = 1.971, and (c) FRF sandwich Abaqus prediction - eigenvalue = 1.935.

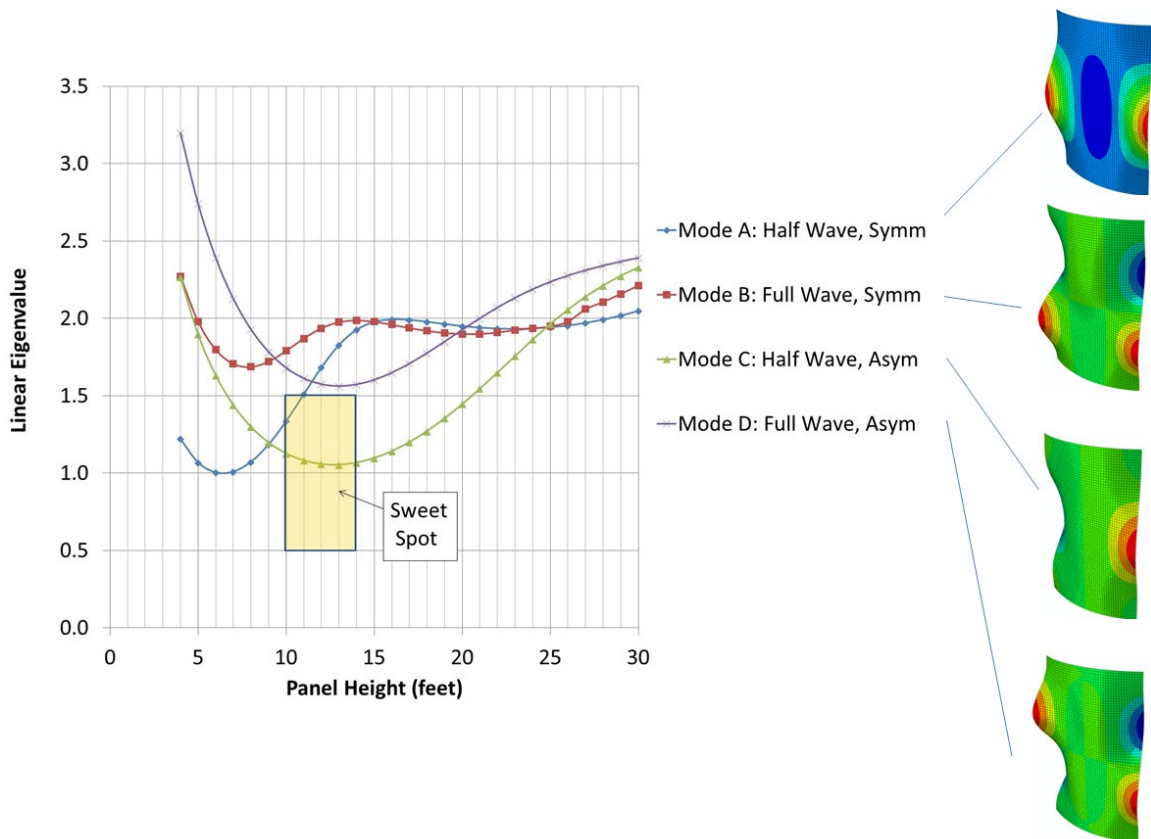


Figure 12.—First four Abaqus-predicted eigenvalues and mode shapes as a function of honeycomb sandwich panel size while maintaining the full panel aspect ratio.

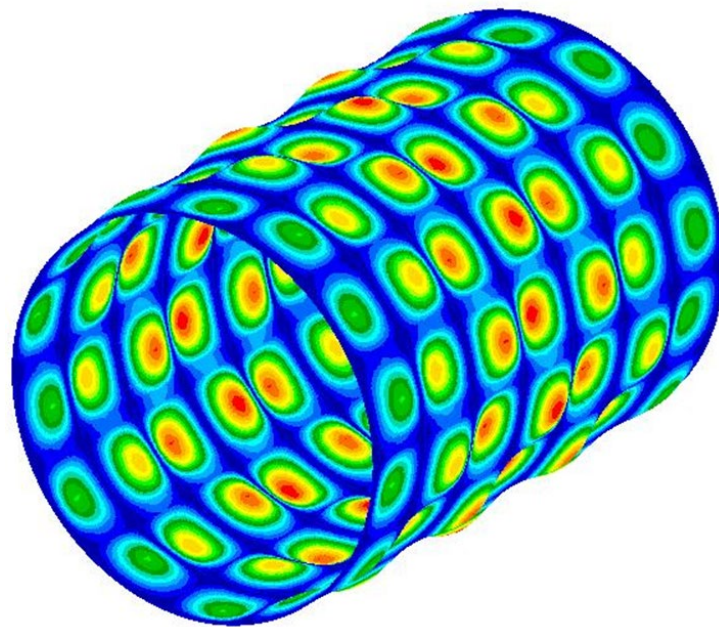


Figure 13.—Buckling mode in a cylindrical, composite honeycomb sandwich shell in axial compression.

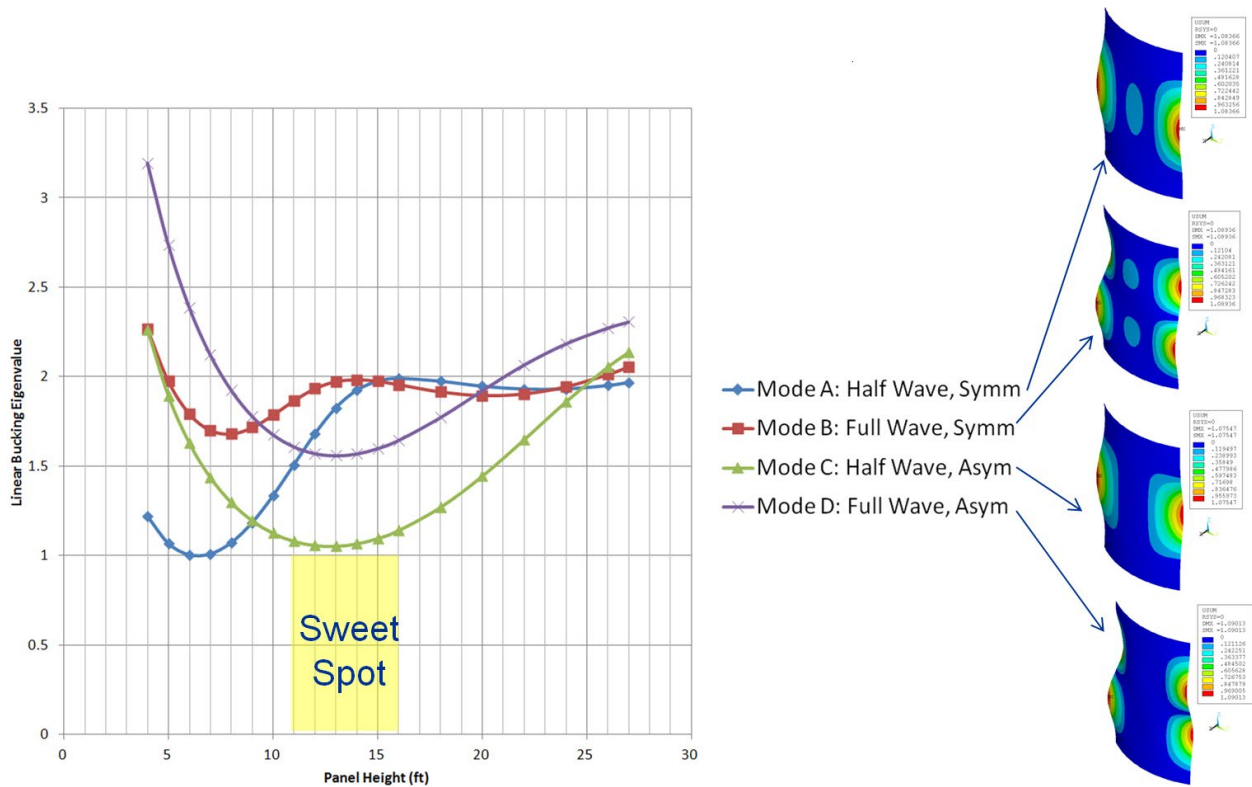


Figure 14.—First four ANSYS-predicted eigenvalues and mode shapes as a function of honeycomb sandwich panel size while maintaining the full panel aspect ratio.

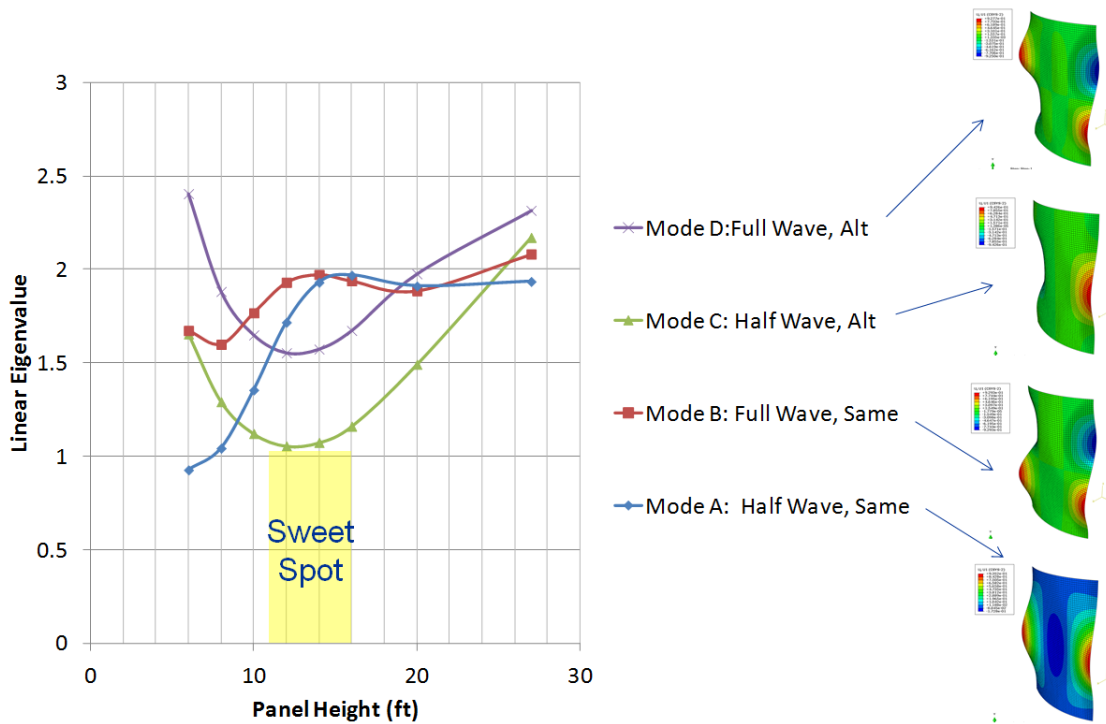


Figure 15.—First four Abaqus-predicted eigenvalues and mode shapes as a function of FRF sandwich panel size while maintaining the full panel aspect ratio.

4.0 Honeycomb Sandwich Panel Nonlinear Buckling Analysis

4.1 Shell Element Based Buckling Analyses

Shell element based, geometrically nonlinear progressive collapse (buckling) analyses were performed for the honeycomb sandwich 1/6th arc-segment panel using ANSYS and Abaqus. In all cases, the first 10 linear eigenvalue buckling modes were used to seed the model with a small degree of geometric imperfection. Then, the actual loading was applied to the geometrically imperfect model in an incremental fashion, with the effects of large displacements activated. The buckling load is then evident as a nonlinearity in the resulting compressive load versus displacement plot for the panel.

It should be noted that, in the case of ANSYS, when performing nonlinear analysis of a structure like the 1/6th panel shown in Figure 10, some sort of imperfection or asymmetry is needed to trigger buckling. That is, if the geometry of the panel is perfect, the applied loading is uniform compression, and the shell properties are such that there is no extensional-bending coupling, then the panel will just compress axially, with no out of plane deformation, even in the presence of nonlinear geometric effects. This is not true in the case of Abaqus (unless the panel is flat), although nonlinear buckling simulations on the perfect geometry can lead to numerical issues. Thus, even for Abaqus, seeding of the model with imperfections is highly desirable.

An alternative method for introducing asymmetry to the model is to apply small perturbations to the applied loads or enforced displacements. This method is not ideal, however, because it is not clear how to realistically introduce such perturbations. For example, varying the load across the top of the panel too drastically could change the problem completely. Another alternative method to introducing geometric imperfections is to slightly modify the coordinates of the nodes with random amplitudes. A disadvantage of using such random imperfections is that they cannot be repeated, and the results would differ for each realization of the same panel. For these reasons, the more straightforward and standard method for imposing geometric imperfections on the finite element model, through use of the linear buckling mode shapes, was employed herein.

Towards this end, the displacements associated with the linear buckling mode shapes is multiplied by a scale factor and added to the initial panel geometry. The scale factor should be on the order of the manufacturing tolerances and thus the initial bowed shape. A factor of 0.020 in. was chosen for the 1/6th panel based on previous work on 3- by 5-ft panels of similar construction (Myers et al., 2013). Either a positive or negative scale factor was used to correctly represent the direction of the initial bow shape of the panels in that study. Without preliminary photogrammetry data of the 1/6th panel, initial imperfections were unknown. Thus, a positive scale factor was used in the Abaqus assessment. Figure 16 shows the first 10 linear buckling mode shapes for the honeycomb sandwich 1/6th arc-segment panel. Figure 17 shows the resulting initial geometry with an exaggerated scale factor for the honeycomb sandwich panel.

Six honeycomb sandwich panel sizes (Figure 18) were analyzed using the nonlinear buckling procedure in both ANSYS and Abaqus. Note that Panel 1 is the full sized 1/6th panel, whereas, Panel 6 is one quarter of the full sized panel. Unlike the linear eigenvalue analysis above, the aspect ratio of all of these panels has not been maintained. The results of the study are shown in Figure 19. In general, the ANSYS and Abaqus result match well. Some differences are evident in the knee region of the curves associated with the initial onset of nonlinear buckling. An example is the 20.25 by 12.95 panel result, where ANSYS appears to have overshot the initial buckling nonlinearity, but after this knee, the results once again match Abaqus. The nonlinear prediction in this knee region appears to be somewhat dependent on the load increment size, which, in these cases, is variable and automatically chosen by ANSYS and Abaqus. Obviously, these codes have different algorithms for determining the increment sizes, which can affect the details of the predicted load—displacement curves.

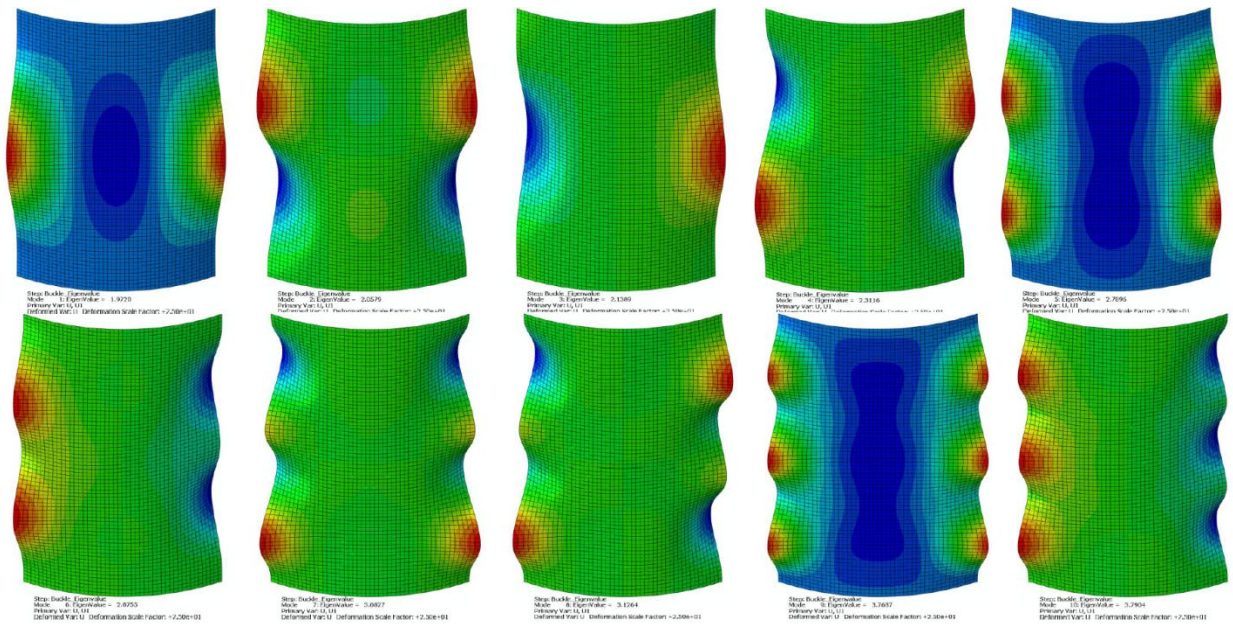


Figure 16.—First 10 linear buckling mode shapes of the honeycomb sandwich 1/6 panel (FRF panel was virtually identical).

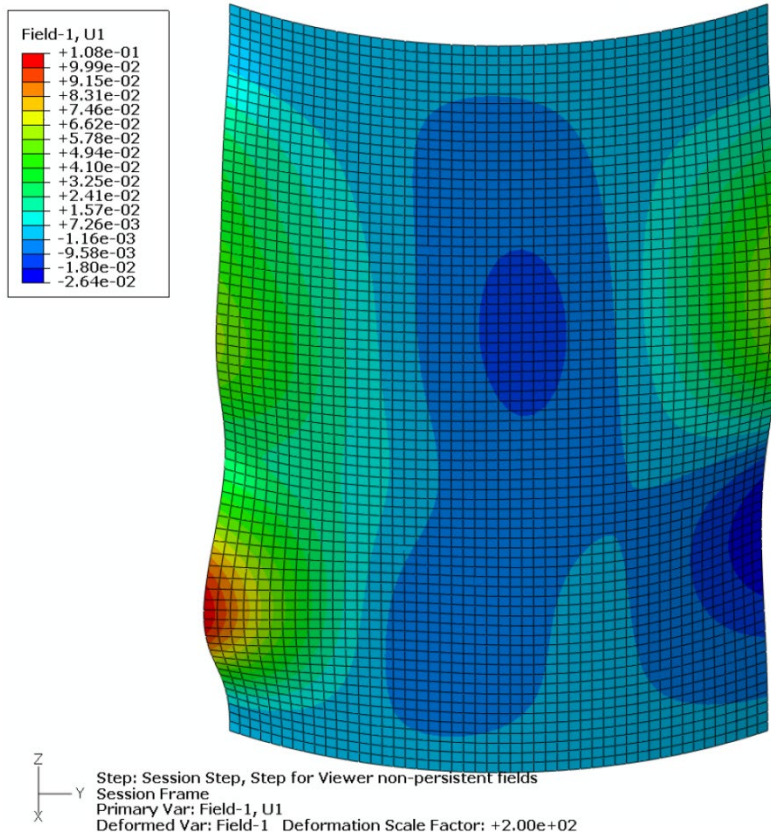


Figure 17.—Initial deformed panel shape with exaggerated imperfections.

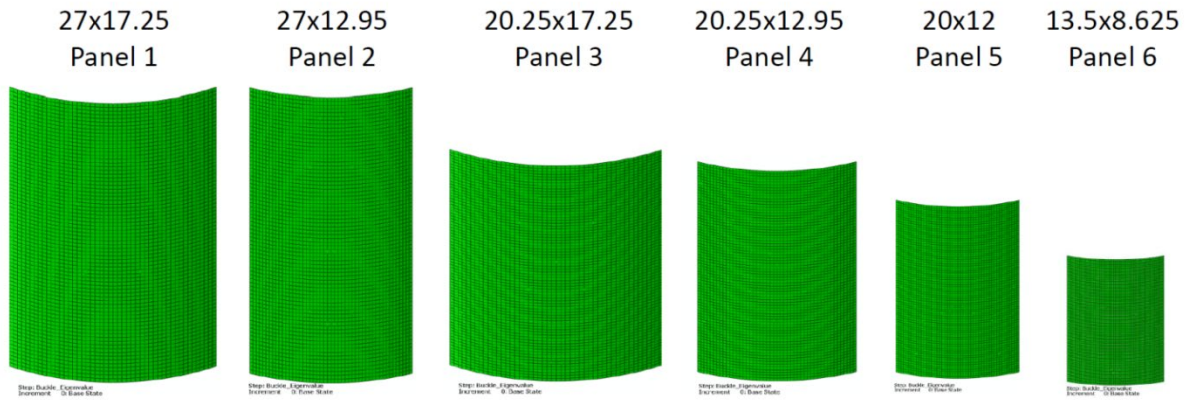


Figure 18.—Sizes of six honeycomb sandwich panels analyzed for nonlinear buckling in ANSYS and Abaqus.

4.2 Solid Element Based Buckling Analyses

The 12- by 7.67-ft arc segment sandwich panel was investigated using two different ANSYS finite element models. The first model was a 2-D layered structural shell element from which the results have been presented earlier. The second model was a 3-D layered structural solid-shell element model in which the test fixturing was also included. In ANSYS, the 2-D layered shell element is called a SHELL281, and the 3-D solid-shell is called a SOLSH190. These finite element types are shown in Figure 20. The SOLSH190 element can be used to model shell structures with a wide range of thickness from thin to moderately thick. Furthermore, the SOLSH190 element formulation permits small thickness to length ratios without producing errors due to large aspect ratios, as can occur in standard solid elements. The thickness between the nodes must equal the sum of the individual layer thicknesses. Otherwise, the software will scale the individual layer thicknesses to fit the actual element thickness. Since the results of the 2-D shell model were included with the Abaqus and ANSYS shell FEM results in previous sections, these results will only be used as a basis of comparison with the 3-D finite element model.

Figure 21 shows the solid-shell model of the test panel geometry with the end plates. For clarity, the finite element edges are suppressed. The panel was modeled as 149-in. tall including the 2.5-in. aluminum end plates and 92-in. wide along the chord. The top and bottom 2.5 in. portions of the panel were supported in the potting material and end plates. Figure 22 shows the slot in the end plate shaped like the arc segment test specimen model. The end of the specimen model is centered in the slot, and the 0.5 in. space around the specimen is filled with solid elements modeling the isotropic UNISORB V-100 potting compound with the elastic properties Young's Modulus (E) of 436 ksi and Poisson's Ratio (ν) of 0.35. Each color represents a different material assignment: cyan for the IM7/977-3 facesheets, purple for the honeycomb core, red for the potting compound, and orange for the aluminum end plates.

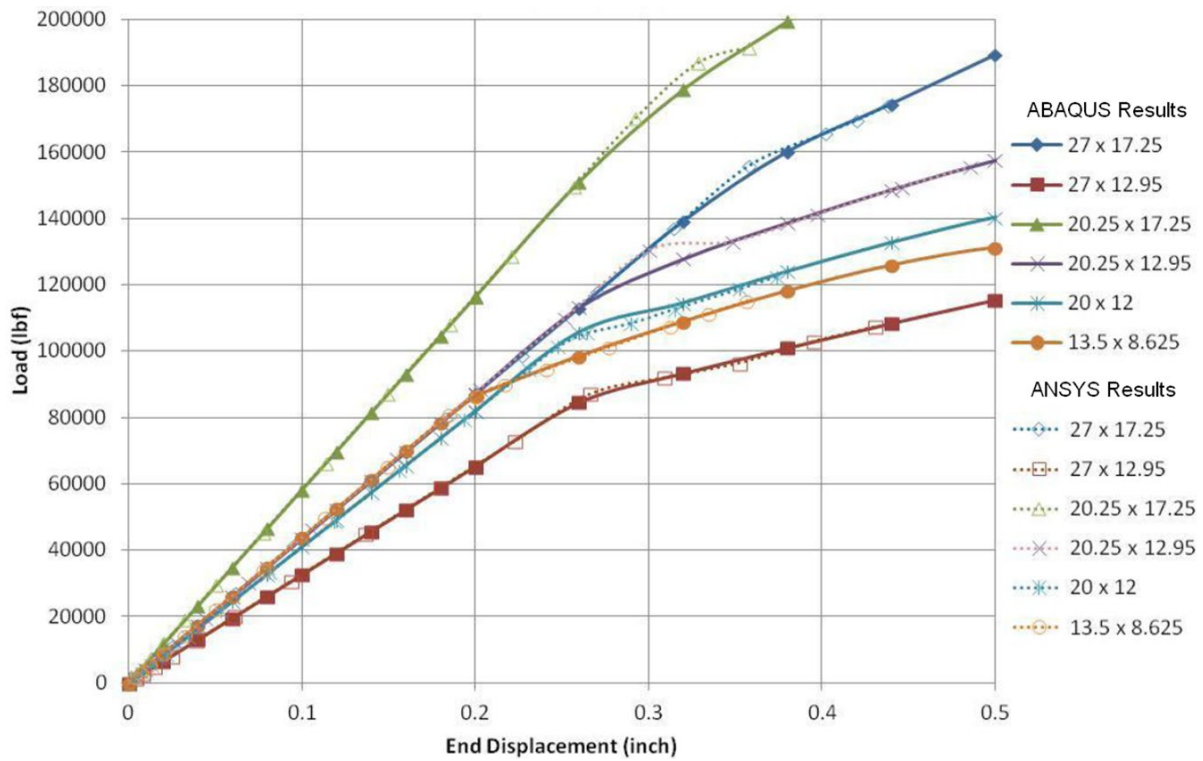


Figure 19.—Nonlinear buckling honeycomb sandwich panel size study. Force versus compression comparisons between Abaqus and ANSYS.

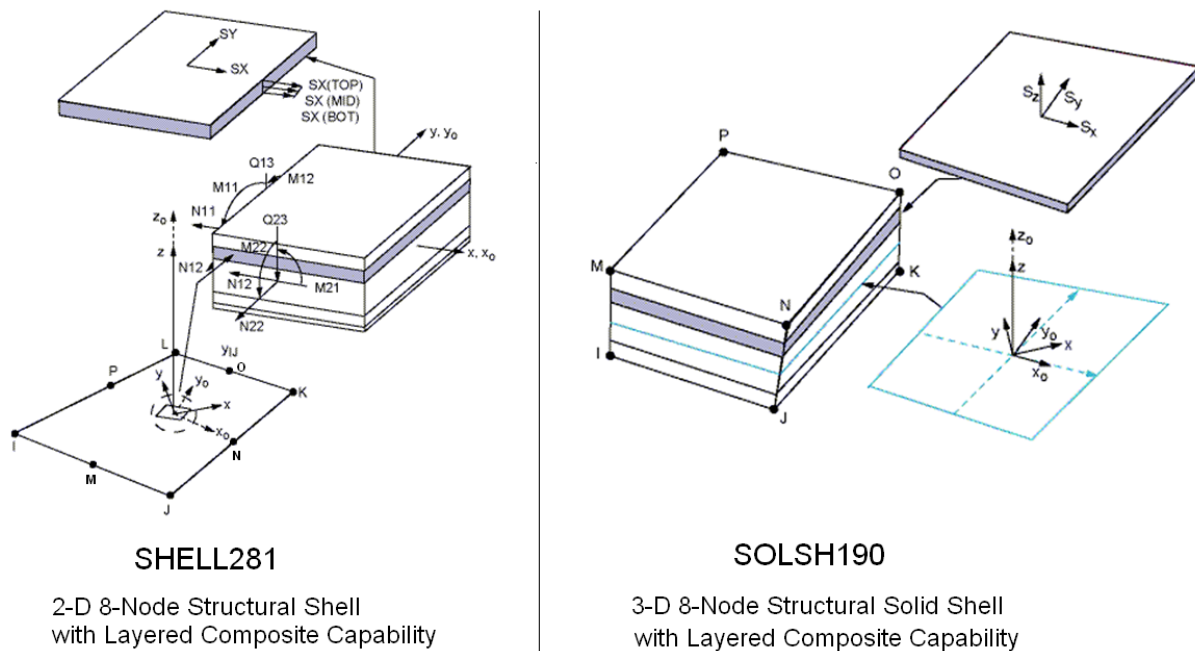


Figure 20.—ANSYS 2-D shell versus 3-D solid-shell (brick) finite elements.

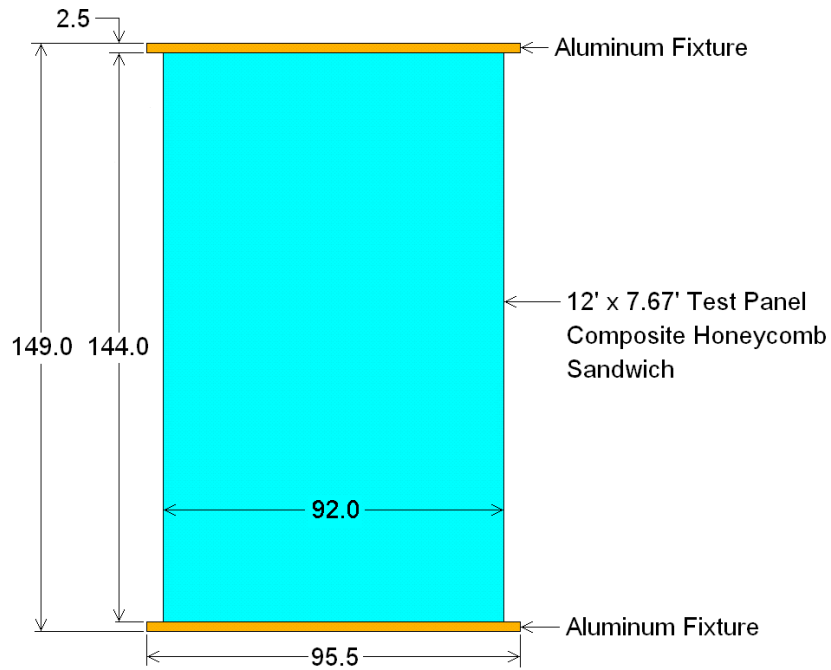


Figure 21.—The 12- by 7.67-ft arc segment test panel configuration.

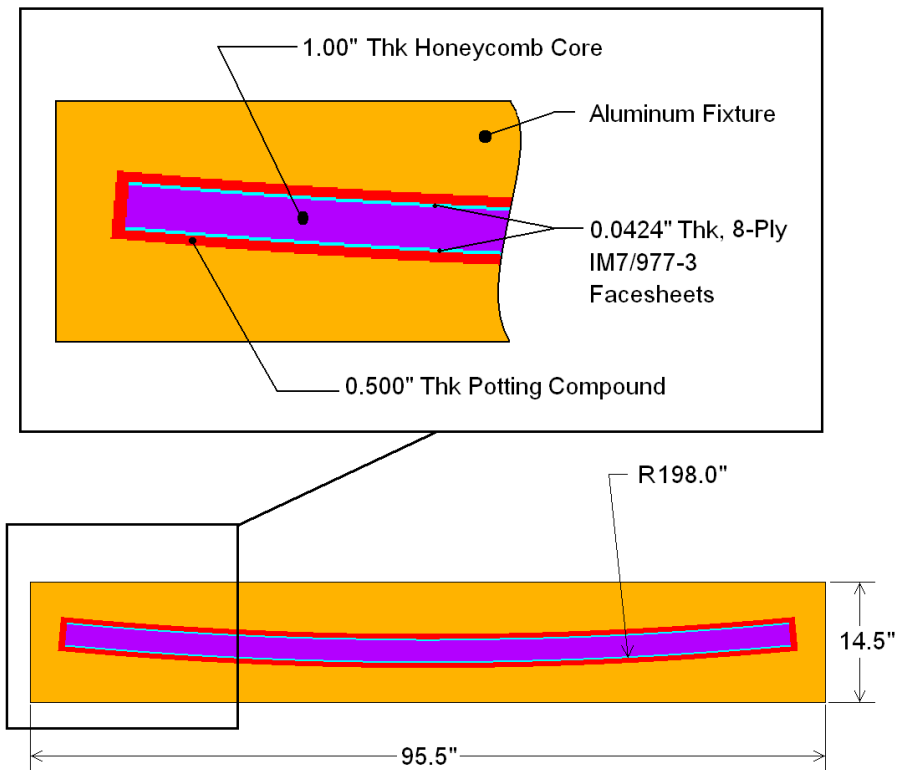


Figure 22.—The 12- by 7.67-ft arc segment test panel and test fixture end view.

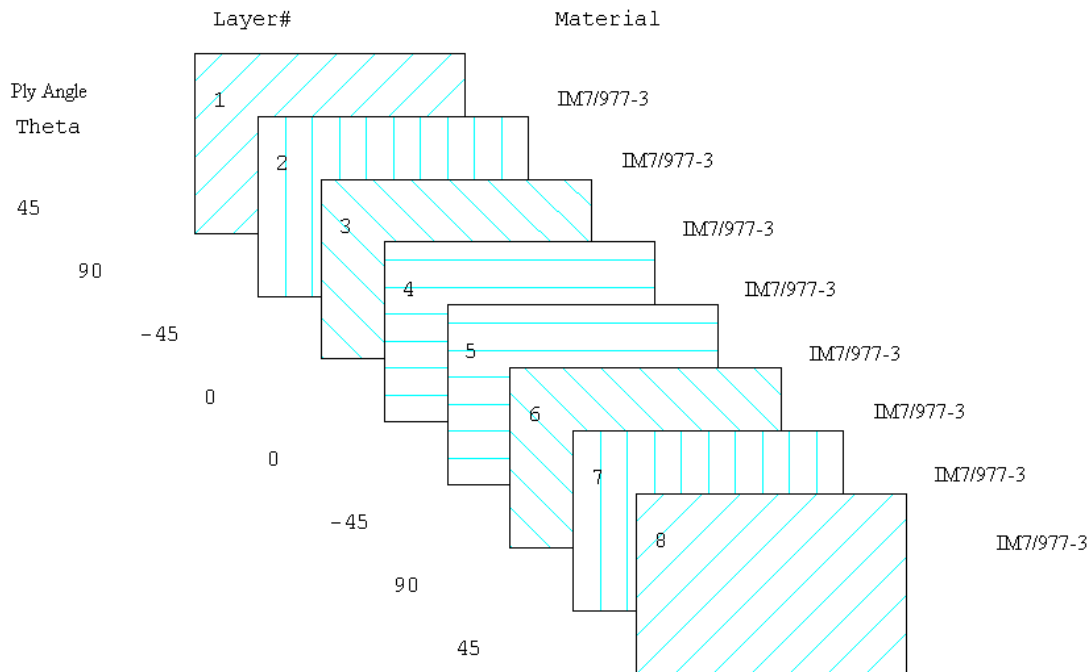


Figure 23.—Facesheet 8-ply stacking sequence.

The solid model was generated using a script file containing ANSYS preprocessing, finite element solution, and post-processing commands in the ANSYS Parametric Design Language (APDL) (ANSYS, 2011). The basic geometry, ply stacking sequence, material properties, and geometric imperfections were defined using parameters. The script file can generate the finite element model, perform each required analysis in sequence, and process the results in tabular or graphic format.

As shown in Figure 23, as in the previous shell finite element models, the stacking sequence of the facesheets was $[45^\circ/90^\circ/-45^\circ/0^\circ]_S$ with 0.0053 in. thick plies. Again, the IM7/977-3 elastic properties and B-basis allowables were obtained from Orion Materials Database (Lockheed Martin, 2010), and they are not listed due to ITAR restrictions. Referring to Table 1, the aluminum (5052-T6 alloy) honeycomb properties were obtained from commercially available literature. Unlike the HyperSizer properties, the honeycomb in-plane longitudinal and transverse moduli (E_1 and E_2) were kept at the actual value of 21.28 psi, and the in-plane shear modulus (G_{12}) was kept at 5.32 psi in the ANSYS solid models. The honeycomb normal (out-of-plane) modulus (E_3) was also kept at 75 ksi.

At the time of writing this report, no tests on the 12- by 7.67-ft honeycomb sandwich panel had been conducted. The actual test panel would be secured between two loading platens, with the bottom end plate fixed on the loading platen. The top end plate would move with the top platen in the axial direction to place the panel in uniaxial compression. Referring to Figure 24, all three displacements in the solid-shell finite element model were fixed along the bottom edge of the panel and end plate. The same boundary condition was applied to the top panel edge and top end plate, except a uniform, monotonic displacement was applied in the negative z-axis direction.

It has been pointed out earlier in this report that the initial geometric imperfections have an impact on the buckling load and direction, especially for an axially compressed, arc segment composite shell structure. The 12- by 7.67-ft curved panel is expected to buckle like a classical full cylinder, with half-wave nodes along the edges. The expected shape is similar to the first linear buckling mode shape shown in Figure 25 and Figure 26. Therefore, the initial imperfect geometry is important to capture in a nonlinear buckling analysis. If the 12- by 7.67-ft panel finite element model is perfectly symmetric (i.e., in geometry and loading), nonsymmetrical buckling does not occur numerically in ANSYS. Rather,

nonlinear buckling analysis fails because nonsymmetrical buckling responses cannot be triggered in such a geometrically perfect finite element model.

As in the nonlinear buckling analysis of the shell-based model, geometric imperfections are obtained by running a preliminary linear buckling analysis, then updating the geometry of the finite element model to the deformed configuration. This technique was implemented by adding the displacements of the first ten mode shapes reduced by a scaling factor. As in the case of the shell-based simulations, a scale factor of 0.020 in. was used for the solid FEM of the 12- by 7.67-ft panel. The shell FEM produced similar linear buckling mode shapes. However, the first mode shape of the shell FEM (Figure 25) was a mirror reflection of the solid FEM's first mode shape (Figure 26). The eighth and ninth modes are also mirror reflections, but the first mode is the desired dominant mode shape for the panel. In order to compare strain results, a negative scale factor (-0.020 in.) was applied to all the modes of the shell FEM. This ensured consistent out-of-plane displacement directions between the two models. Figure 27 shows the solid FEM perfect and exaggerated imperfect geometries.

After the geometric imperfections were added to the finite element model, the nonlinear buckling analysis was performed. In ANSYS, a nonlinear buckling analysis is a static analysis with large deflections active. The magnitude of the applied axial compression is extended beyond the first linear (Eigen) buckling mode. In this analysis the compression was increased gradually using 50 small time increments to predict the critical buckling load. Figure 28 shows the reaction load versus end compression for the linear and nonlinear shell and solid ANSYS models of the 12- by 7.67-ft panel. The two linear buckling analyses appear to over-predict slightly the buckling loads predicted by the two nonlinear analyses. In both nonlinear ANSYS analyses, the panel initial stiffness was nearly the same.

Figure 29 shows the panel radial displacement plot (radial component of the total displacement field) when -0.221 in. was applied to the top edge, which is after the buckling knee apparent in Figure 28. This figure shows that the geometric imperfections applied to the model are dominated by the first linear buckling mode shape (see Figure 26). As expected, the 12- by 7.67-ft arc-segment honeycomb sandwich panel buckles with circumferential waves rather than in a column-like mode.

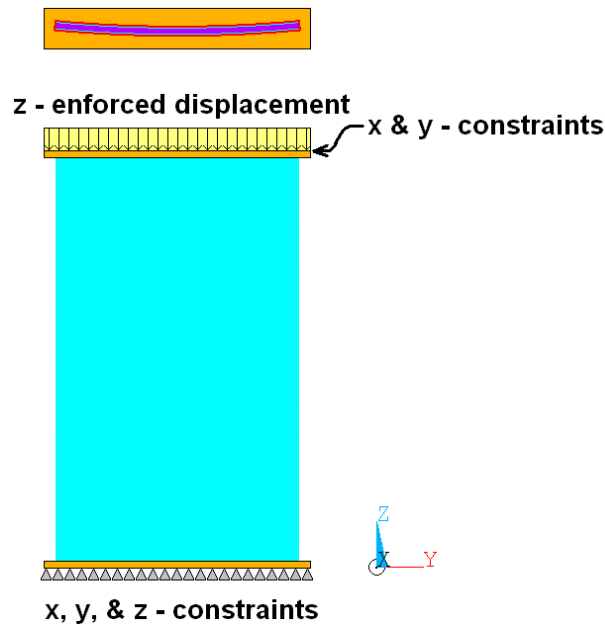


Figure 24.—ANSYS Solid Model boundary conditions.

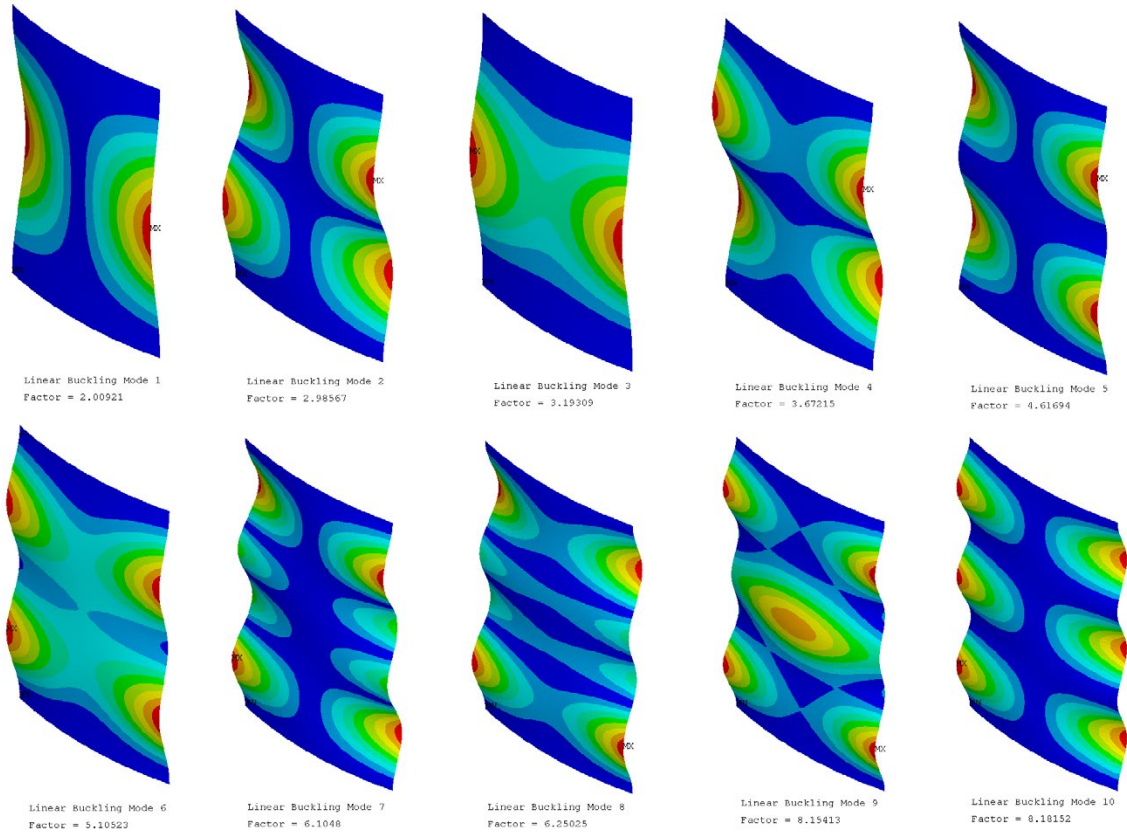


Figure 25.—First 10 linear buckling mode shapes for the ANSYS Shell FEM

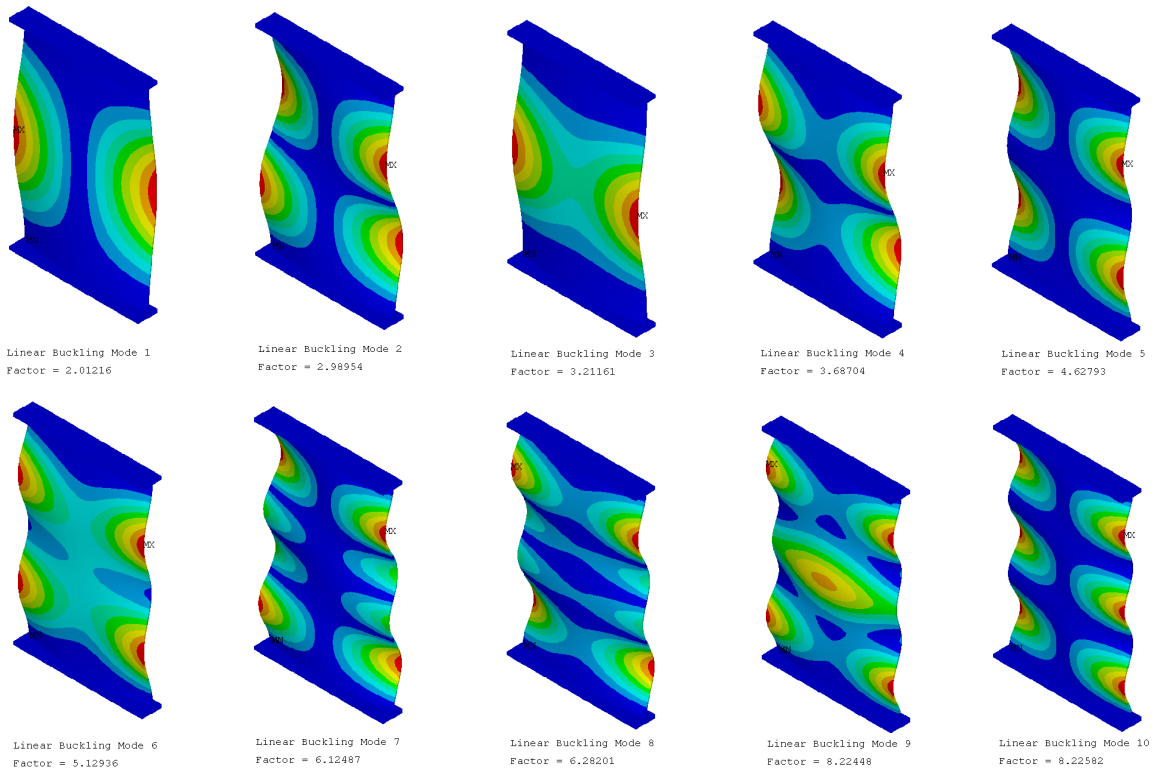


Figure 26.—First 10 linear buckling mode shapes for the ANSYS Solid FEM.

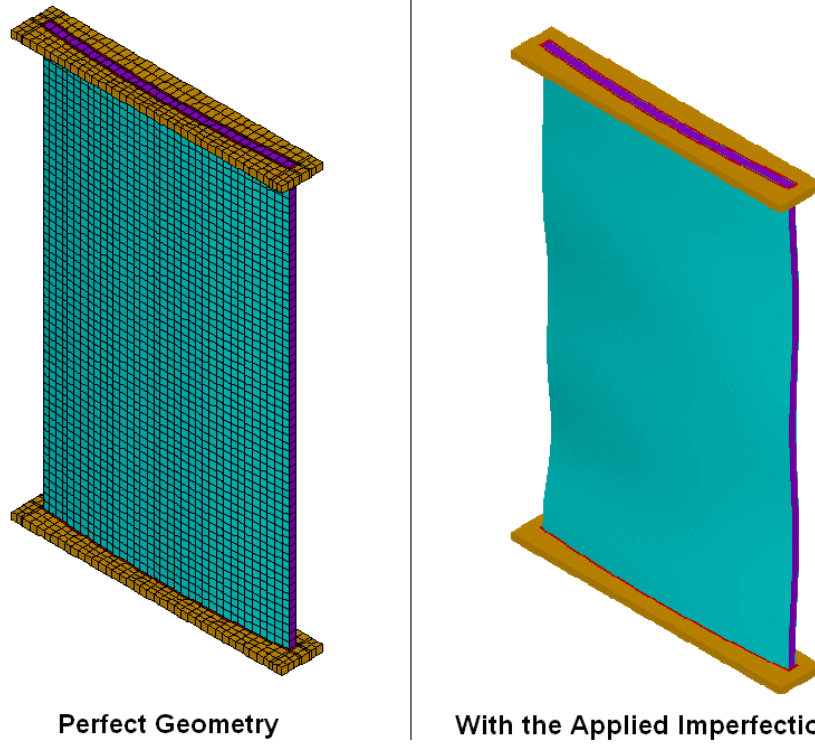


Figure 27.—Panel model with the applied geometric imperfections (exaggerated).

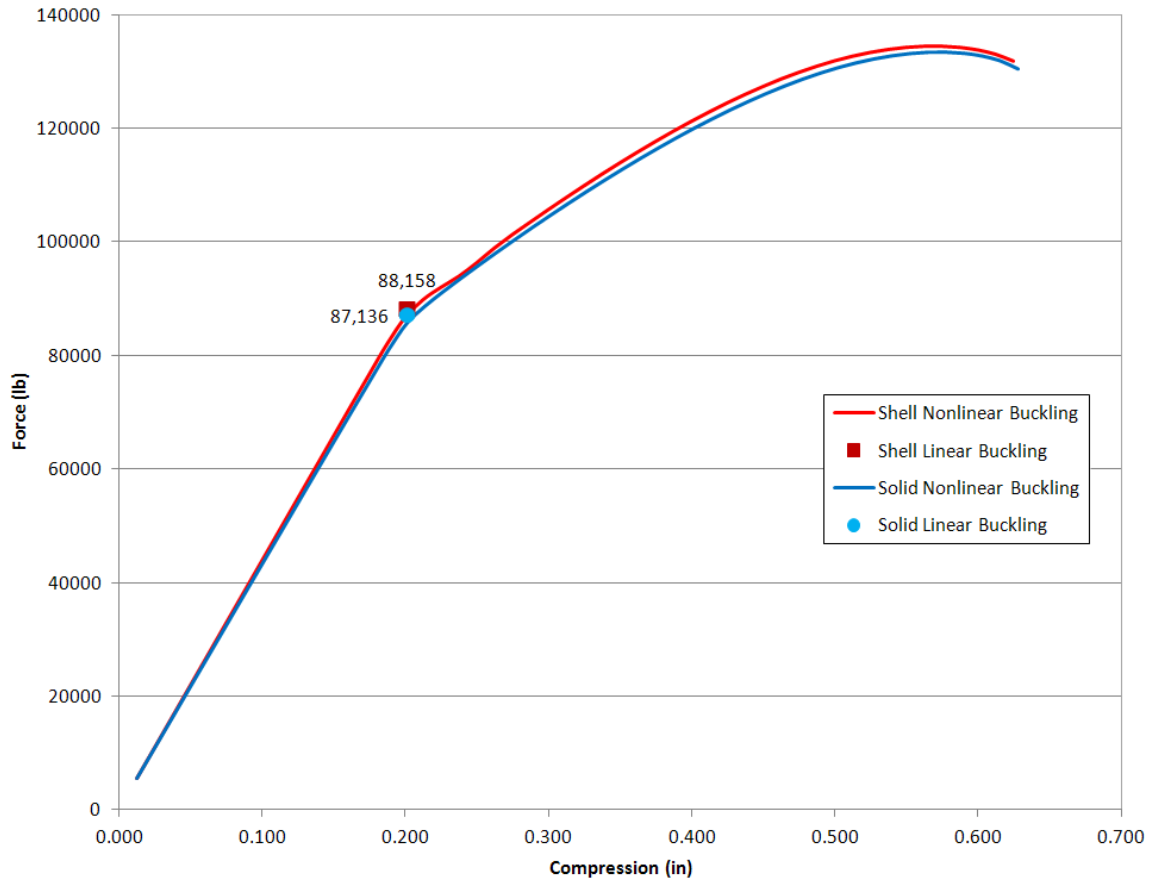


Figure 28.—Total reaction load versus end shortening for ANSYS Solid FEM.

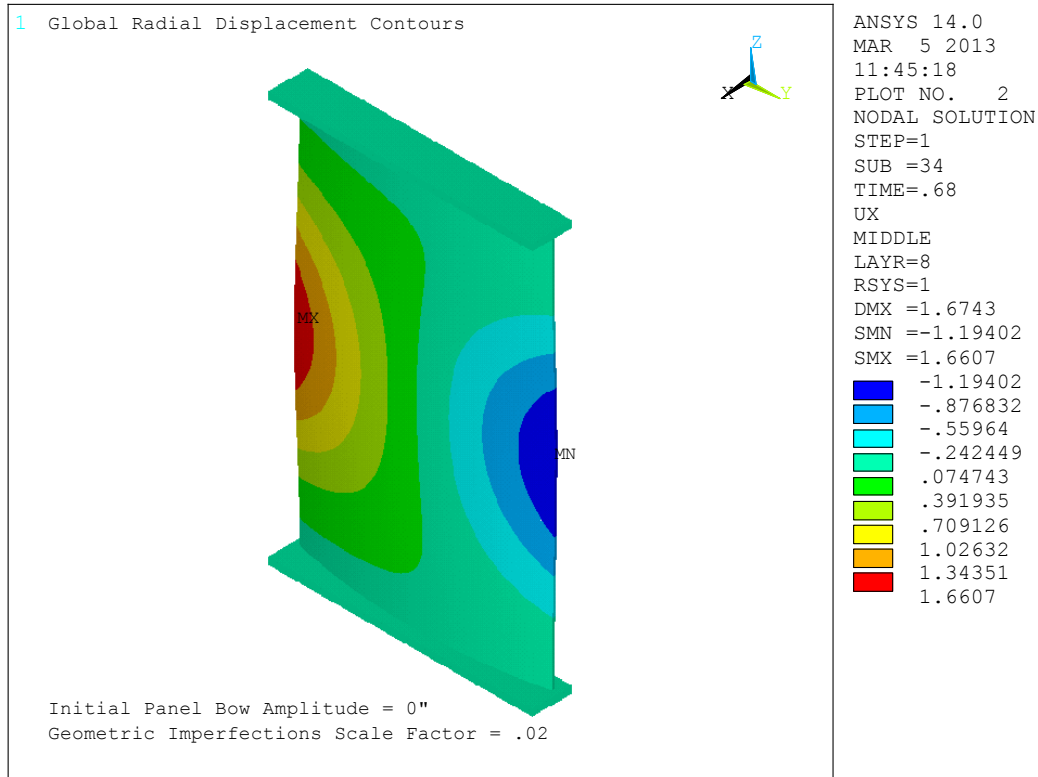


Figure 29.—ANSYS Solid FEM, post-buckling radial displacement contour plot at 0.221-in. end shortening (90,094 lb).

Potential strain gage locations for the 12- by 7.67-ft arc-segment honeycomb sandwich panel are shown in Figure 30. These gage locations were used to extract local strain data from the ANSYS solid and shell FEMs.

Figure 31 shows load versus minimum principal strain plots for both the solid FEM and shell FEM at gages 15 and 16 near the left edge at the vertical centerline. The plots confirm that applying a negative scale factor to the imperfections (linear buckling modes) of the shell FEM produced similar results to the solid FEM.

An additional analysis was performed on the solid FEM of 12- by 7.67-ft panel to refine the ANSYS results near the predicted buckling load. In this analysis the compression was increased gradually using 50 small time increments up to 0.325 in., which was just beyond the compression of 0.201 in. predicted by the linear buckling analysis. Note that this increment size is approximately one-half of that used previously (e.g., in Figure 31). A plot of the load versus compression in Figure 32 shows the additional refinement in the results. Figure 33 shows how the load versus compression results from the refined analysis compare with the original analysis results. The main purpose in the refinement was to capture more strain data near the predicted buckling load.

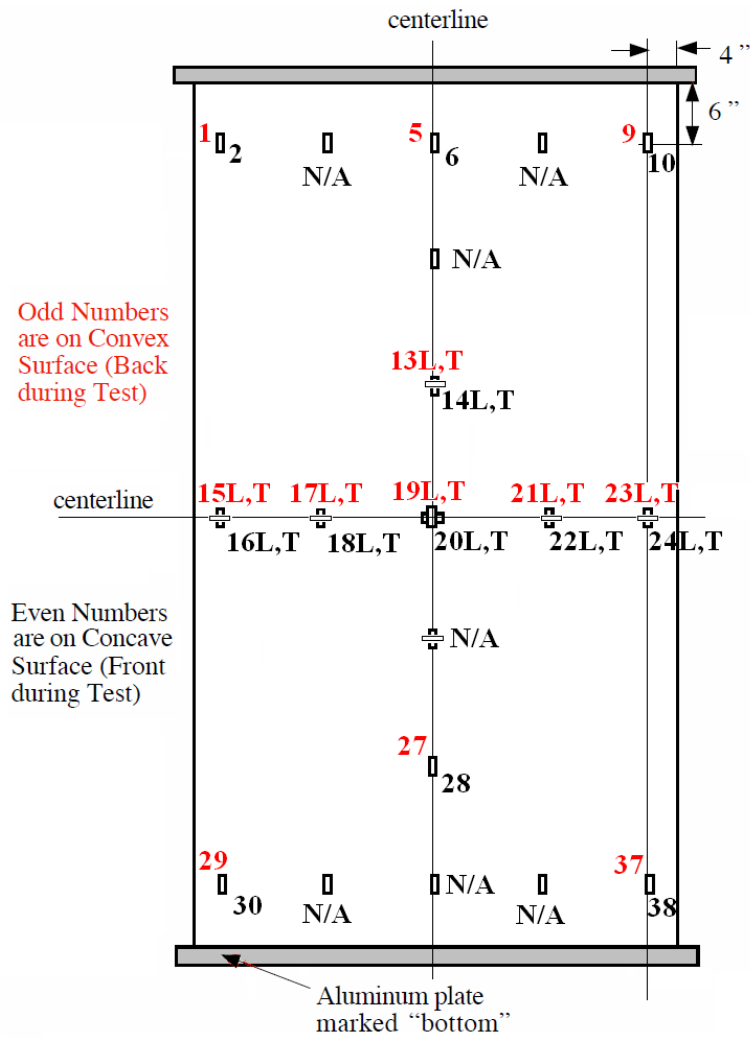


Figure 30.—Proposed strain gage locations for the 12- by 7.67-ft honeycomb sandwich composite panel, (odd (OML), even (IML)).

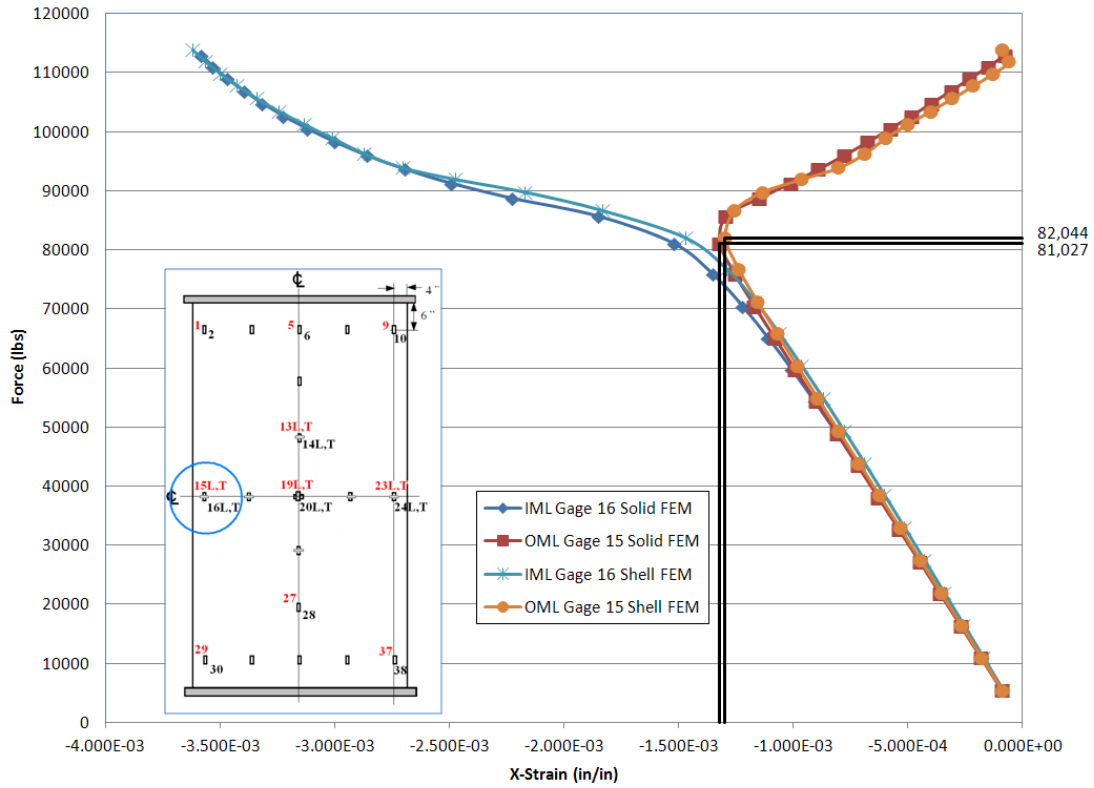


Figure 31.—Load versus minimum principal strain plots for solid versus shell FEM at gages 15 and 16.

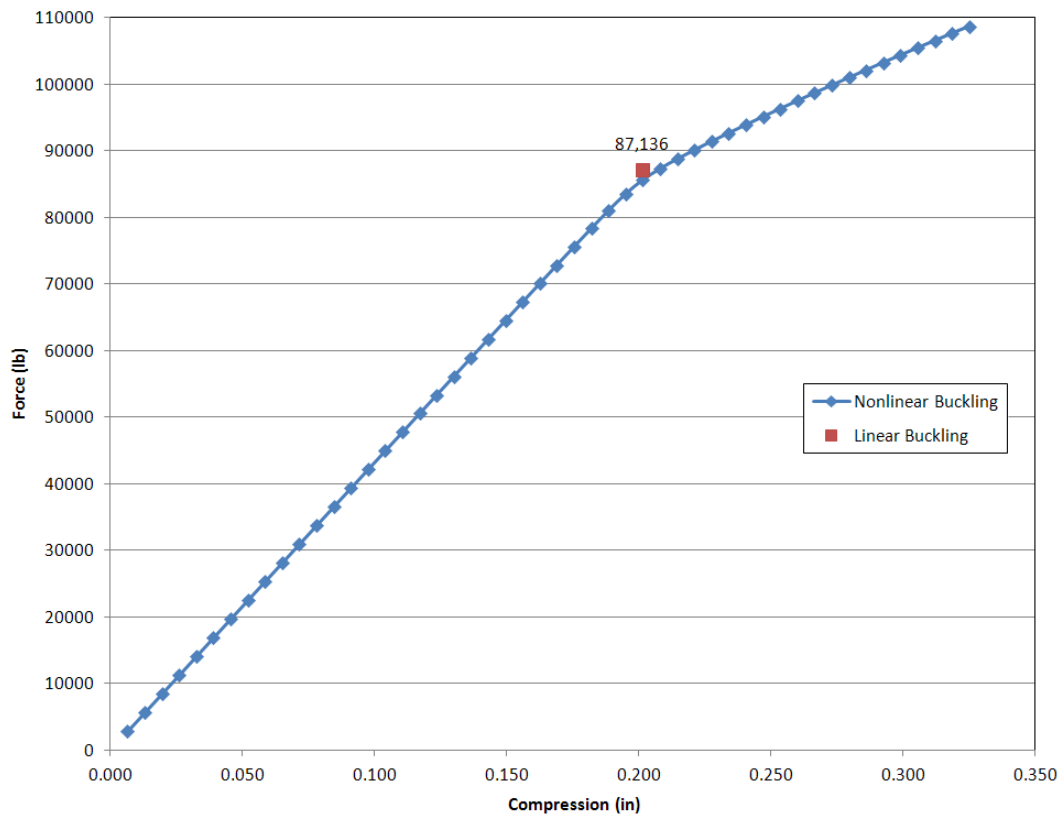


Figure 32.—Total reaction load versus end shortening for the ANSYS Solid FEM (refined analysis).

To determine the panel buckling loads, a method from Singer et al. (1998), shown in Figure 34, was used. This method utilizes global load versus local axial strain gage data to determine the onset of buckling. In Figure 34, a vertical tangent line intersects the load-strain curve at a local strain where the local strain increment reverses. The load corresponding to that local strain is designated the local buckling load, with the lowest local buckling load indicating the panel buckling initiation load. It should be noted that the buckling strain, and hence buckling load, can only be determined at monitored locations and therefore a value lower than the lowest detected value could be present. Thus, the postulated buckling initiation load is somewhat subjective and based upon the location where the strains are being monitored for reversal

The strains in the curved panel are, in general, three dimensional. In a panel compression test, strains are typically measured on a free surface using strain gages or digital image correlation techniques. Max and min principal strains are frequently used to assess structural integrity in conjunction with the finite element method because they provide a convenient scalar quantity representing an extreme that can be plotted over the structure. Principal strains, however, are influenced by the entire strain field. Thus, where significant shear strains are present, such as in the panel corners and near the buckling wave inflection points, the principal strains can deviate from the global axial and tangential strains. Far from the panel ends, and away from inflection points, shear strains are minimal, and the principal strains should correspond to the axial and tangential strains. To examine this potential effect, the minimum principal strains, axial strains, and z-strains were plotted on each surface in Figure 35 and Figure 36 at a 0.2145-in. end compression of the panel.

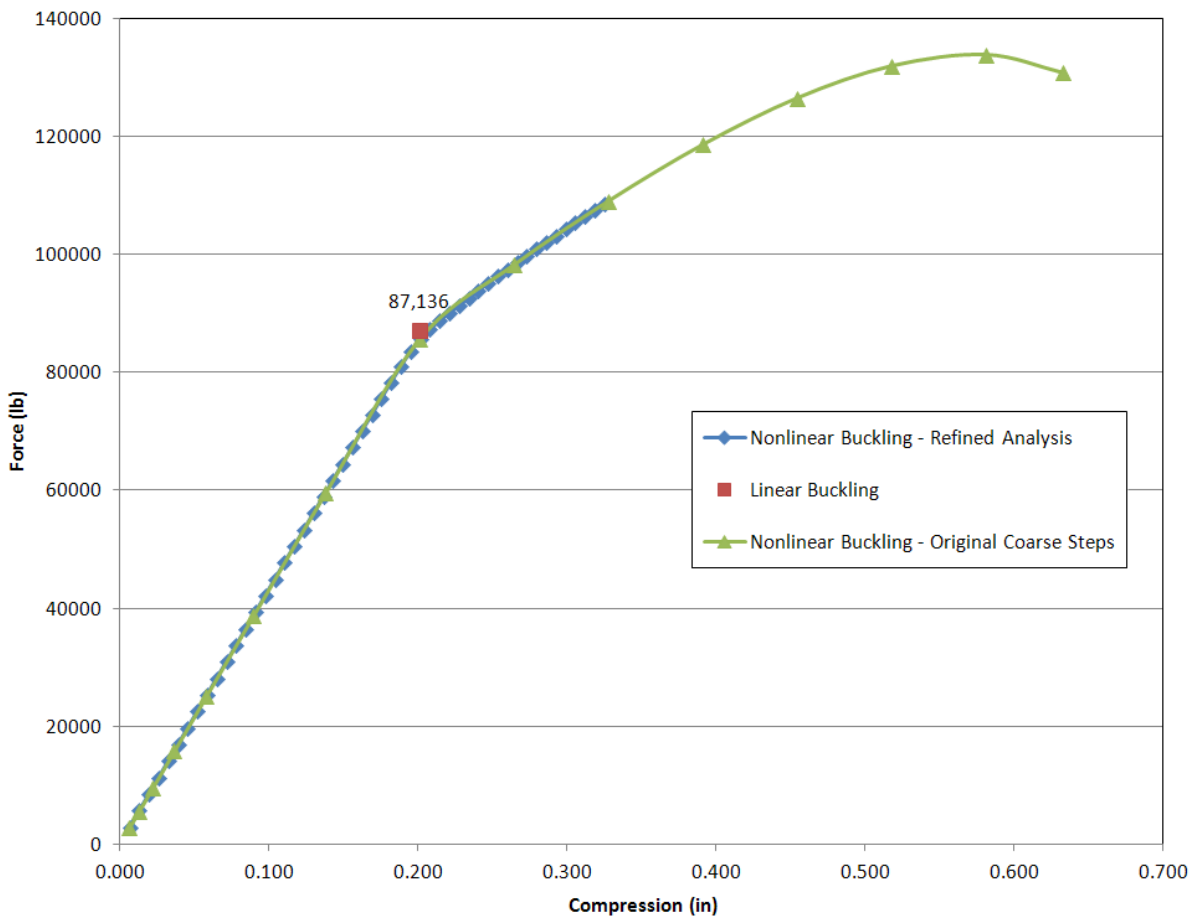


Figure 33.—Refined versus original coarse load step, buckling analysis.

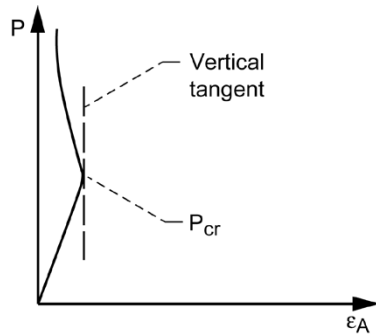


Figure 34.—Method for determining buckling load from Singer et al. (1998).

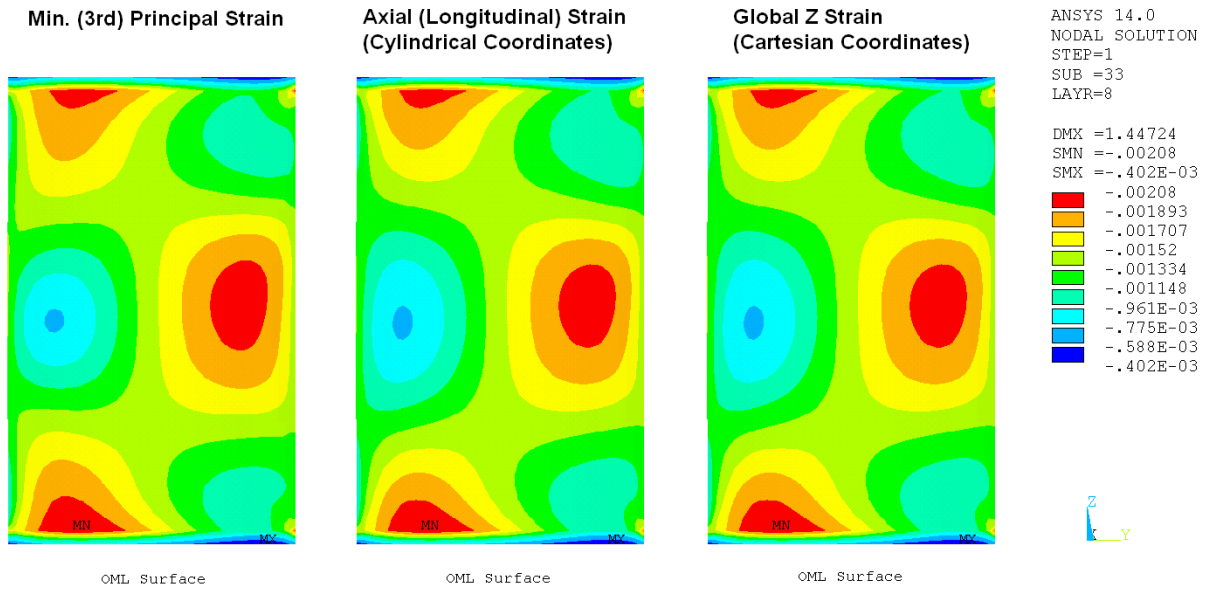


Figure 35.—Minimum principal and component strain comparisons on the OML surface at 0.2145-in. compression.

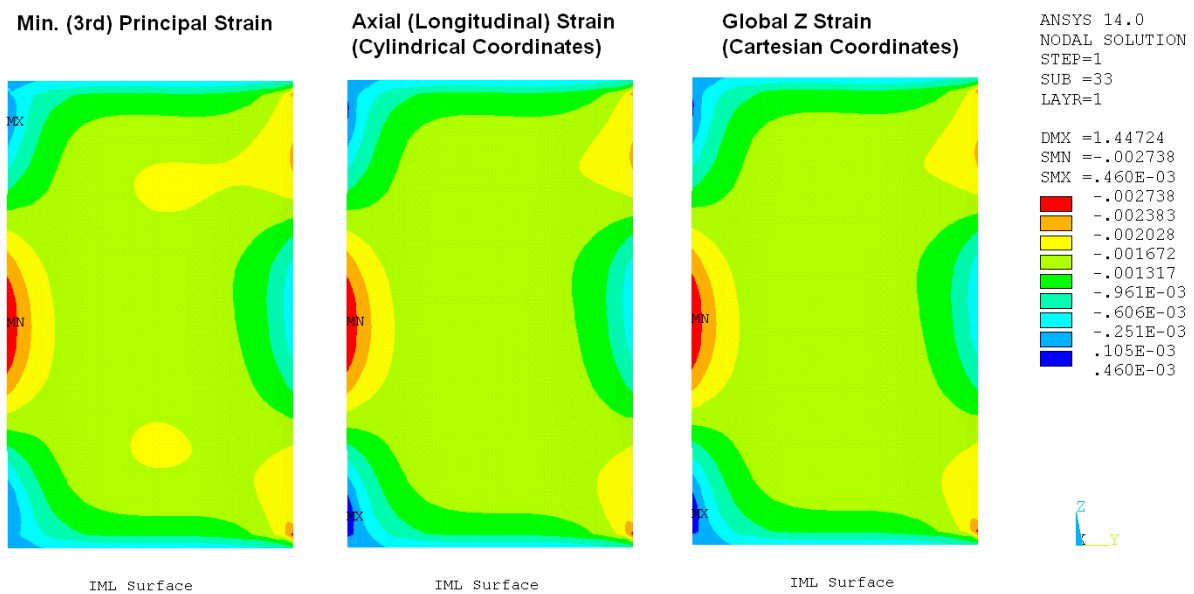
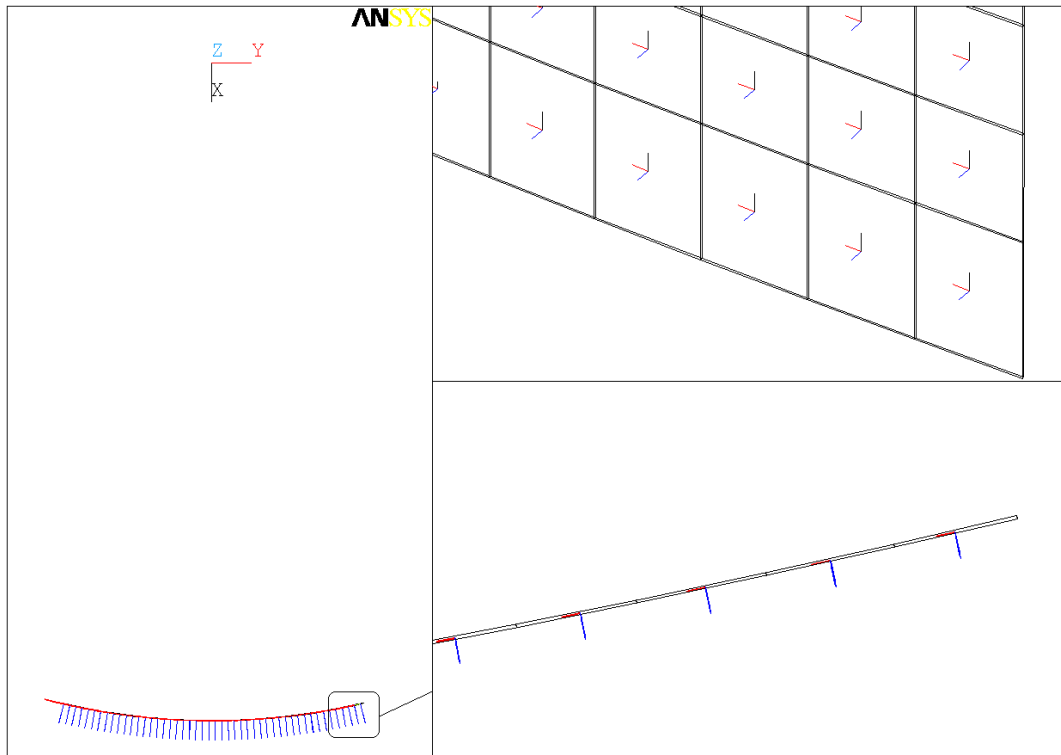


Figure 36.—Minimum principal and component strain comparisons on the IML surface at 0.2145-in. compression.



12x7.667 HC Panel, 8-Ply, IM7/977-3 Face Sheets, 0" Bow

Figure 37.—Element coordinate systems for the OML facesheet elements.

Both Figure 35 and Figure 36 show little variations in the strain contours. The ANSYS time history post-processing module warns the user of potential problems extracting data from the structural solid-shell finite elements with layered composite capability. Averaging performed in the module assumes consistent coordinate systems for all the elements used in the averaging. This is not a condition required by the general post-processing module which was used to produce the contour plots. The model generated for this paper aligned each element coordinate system with the axial direction in order to define ply angles along the fiber directions. Furthermore, one axis of each element coordinate system is also aligned with the surface normal as shown in Figure 37 in which only the OML facesheet elements have been selected. This led to incorrectly averaged nodal results for component strains (x , y , or z) because the strains in each layer were in different reference frames. However, principal strains are independent of the element coordinate systems, and the averaged nodal results for the principal strains should be representative, although different for each ply. Thus, the min. principal strains in the 12- by 7.67-ft panel were used instead of the axial strains in Singer's method for determining the onset of buckling.

Buckling loads as indicated by the various strain gage pairs using the method of Singer et al. (1998) are tabulated in Table 5. All strain gage pairs are listed, but some strain gage pairs did not exhibit a strain reversal. The first detected minimum principal strain reversal occurs at the location of gages 1 and 2 located near the top left corner of the panel and the location of gages 29 and 30 located near the lower left corner of the panel, at a load of 75,598 lb. Figure 38 to Figure 49 show plots of the load versus minimum principal strain for all strain gage pairs. Figure 38 and Figure 48 show that, in the left corners, the IML panel strains went into compression up to the onset buckling, after which the strain increment reverses and the axial strain is alleviated as the load increases during post-buckling. However, Figure 40 and Figure 49 show that, in the right corners, the OML panel strains went into compression up to the onset buckling, after which the strain increment reverses and the strain is alleviated as the load increases. Furthermore, Figure 42 and Figure 43 show that, near the left edge in the panel vertical center, the OML panel strains went into compression up to the onset buckling, after which the strain increment reverses.

Near the right edge at the panel vertical center, Figure 45 and Figure 46 show that axial IML panel strains went into compression up to the onset buckling, after which the strain increment reverses. Figure 44 shows that there is no strain reversal at the panel center, and Figure 39 shows no strain reversal at the panel top center. The panel vertical center lies at an inflection point, as shown by the radial displacement contour plot in Figure 29. These panel strain results are consistent with the solid FEM buckling mode shown in Figure 29. The strains at gages 13, 14 (Figure 41) and gages 27, 28 (Figure 47) show no strain reversal.

TABLE 5—PREDICTED BUCKLING LOADS FROM THE SOLID FEM ANALYSIS

Gage	Analysis results, lb	Microstrain
1,2	75,598	1006
5,6	-----	-----
9,10	85,617	1431
13,14	-----	-----
15,16	81,008	1277
17,18	81,008	1149
19,20	-----	-----
21,22	106,533	1525
23,24	78,333	1239
27,28	-----	-----
29,30	75,598	858
37,38	85,617	1359

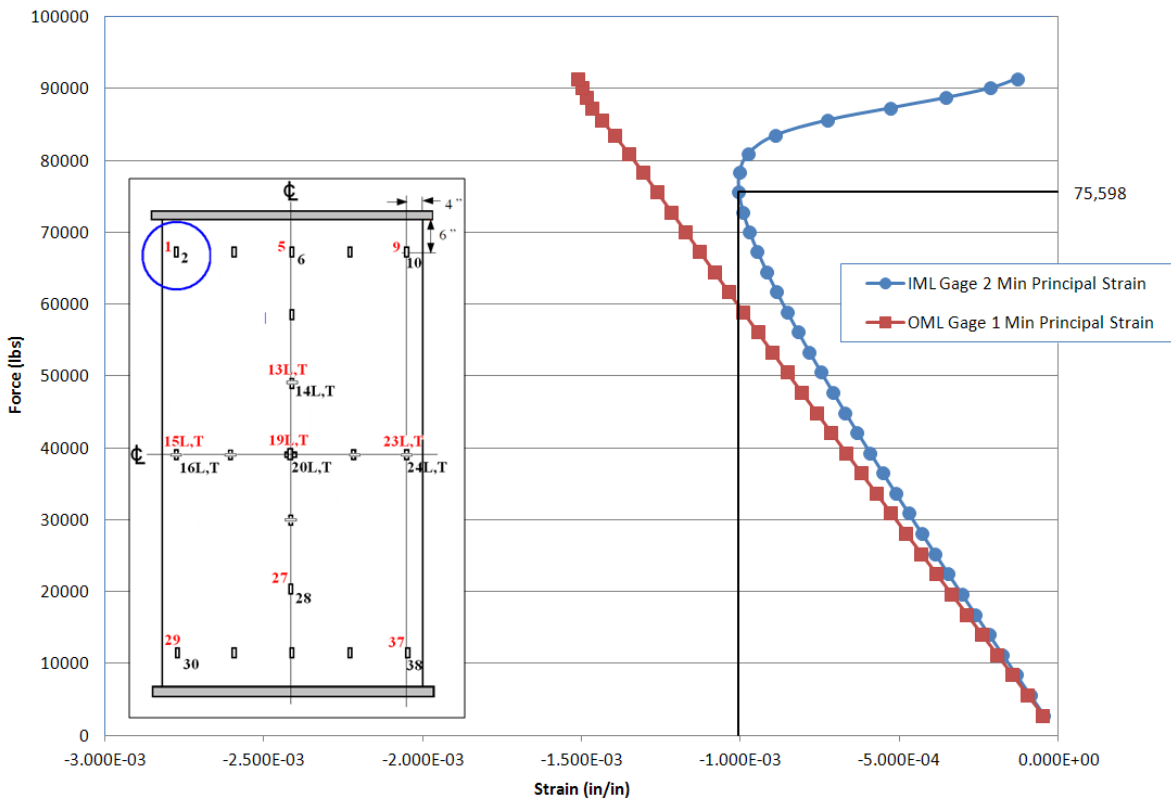


Figure 38.—Load versus minimum principal strain plots for gages 1 and 2.

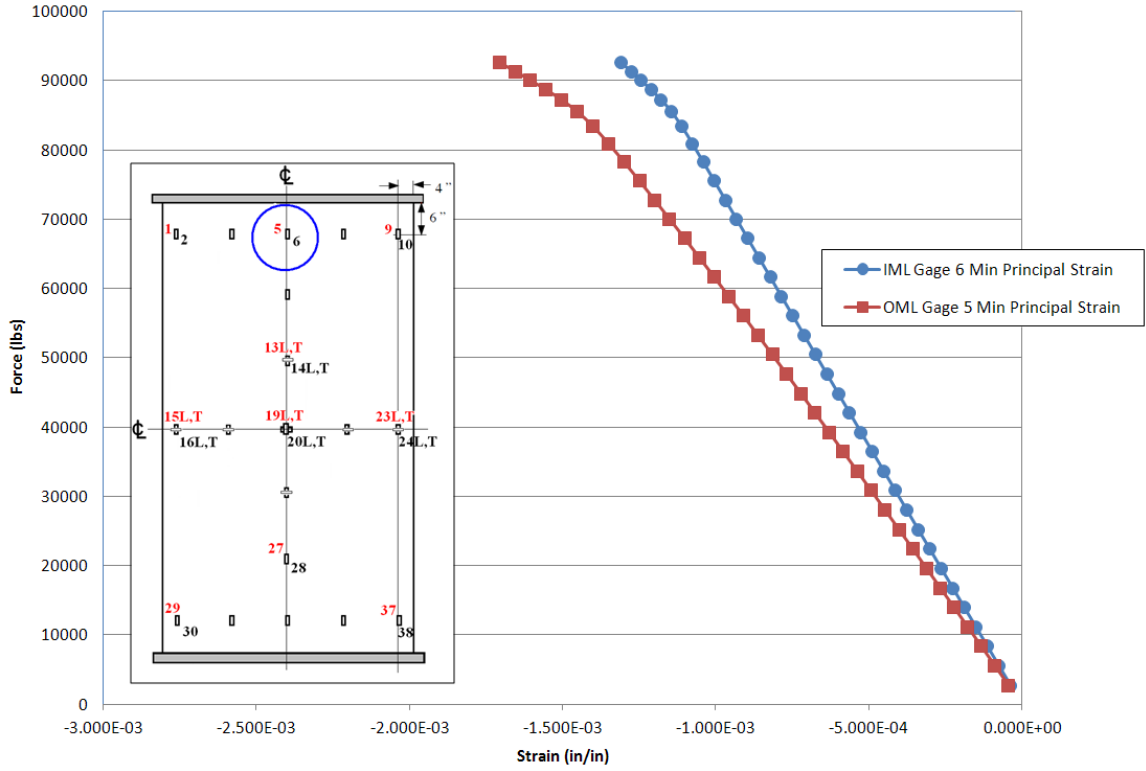


Figure 39.—Load versus minimum principal strain plots for gages 5 and 6.

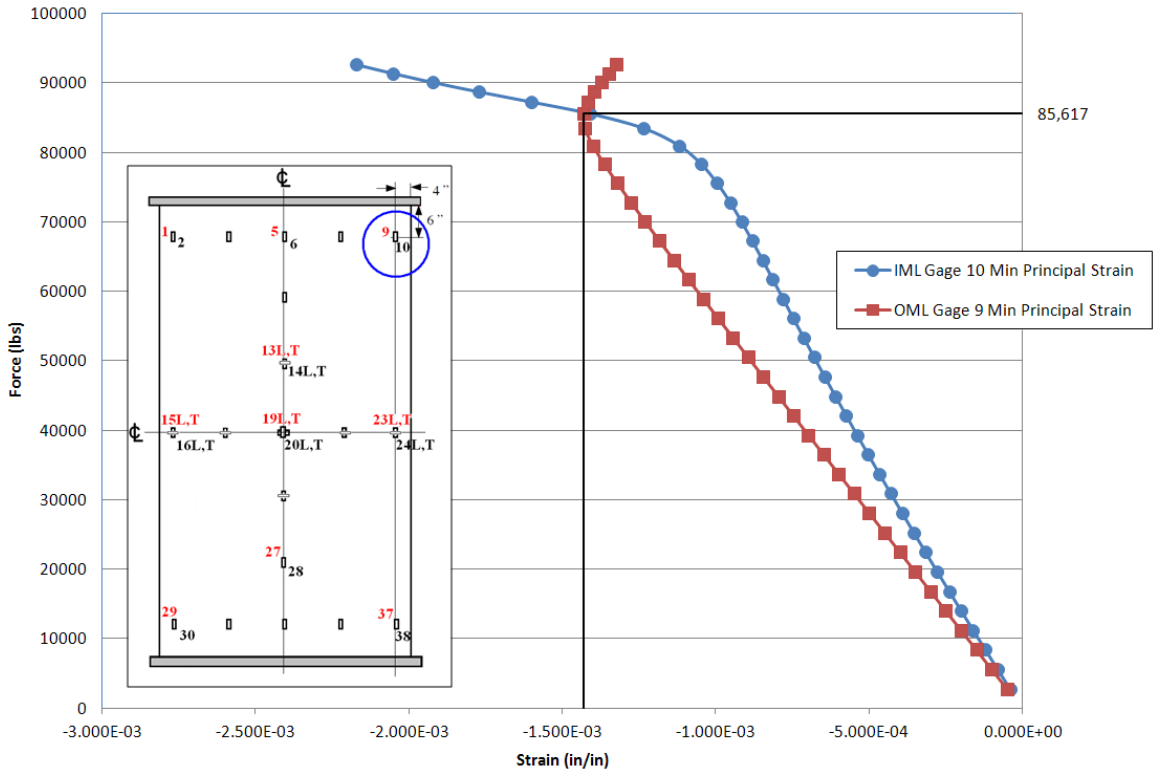


Figure 40.—Load versus minimum principal strain plots for gages 9 and 10.

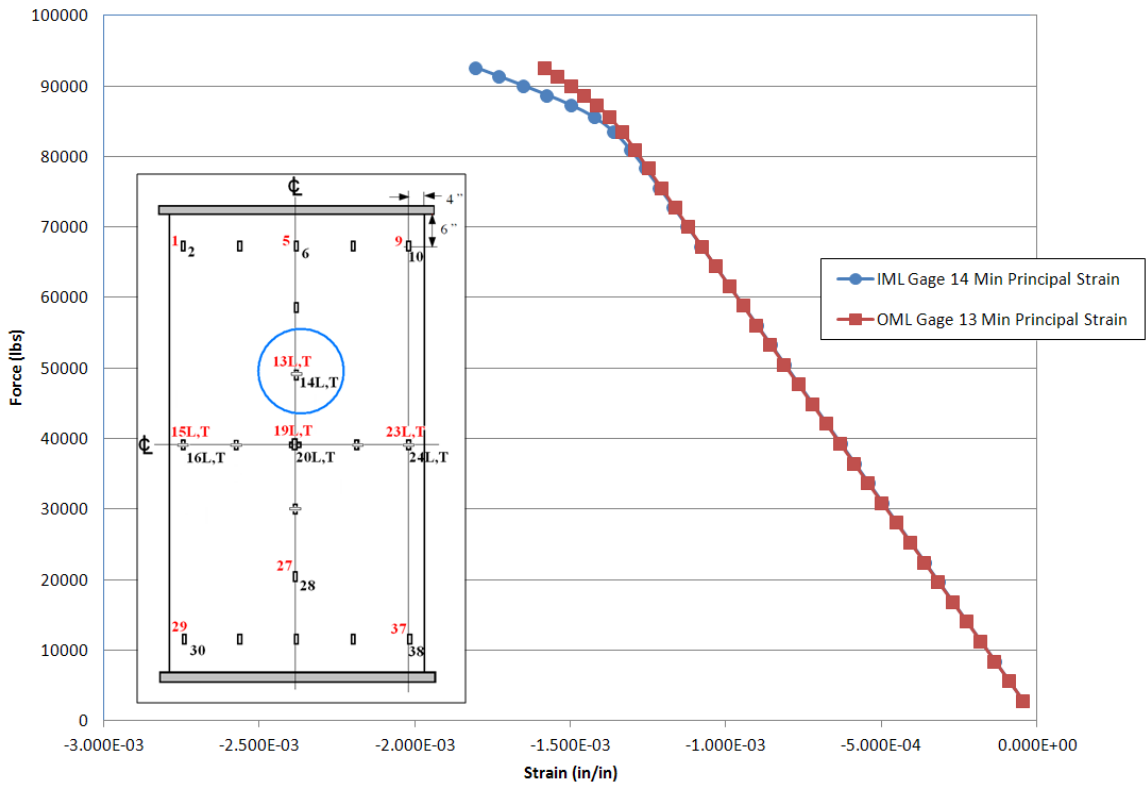


Figure 41.—Load versus minimum principal strain plots for gages 13 and 14.

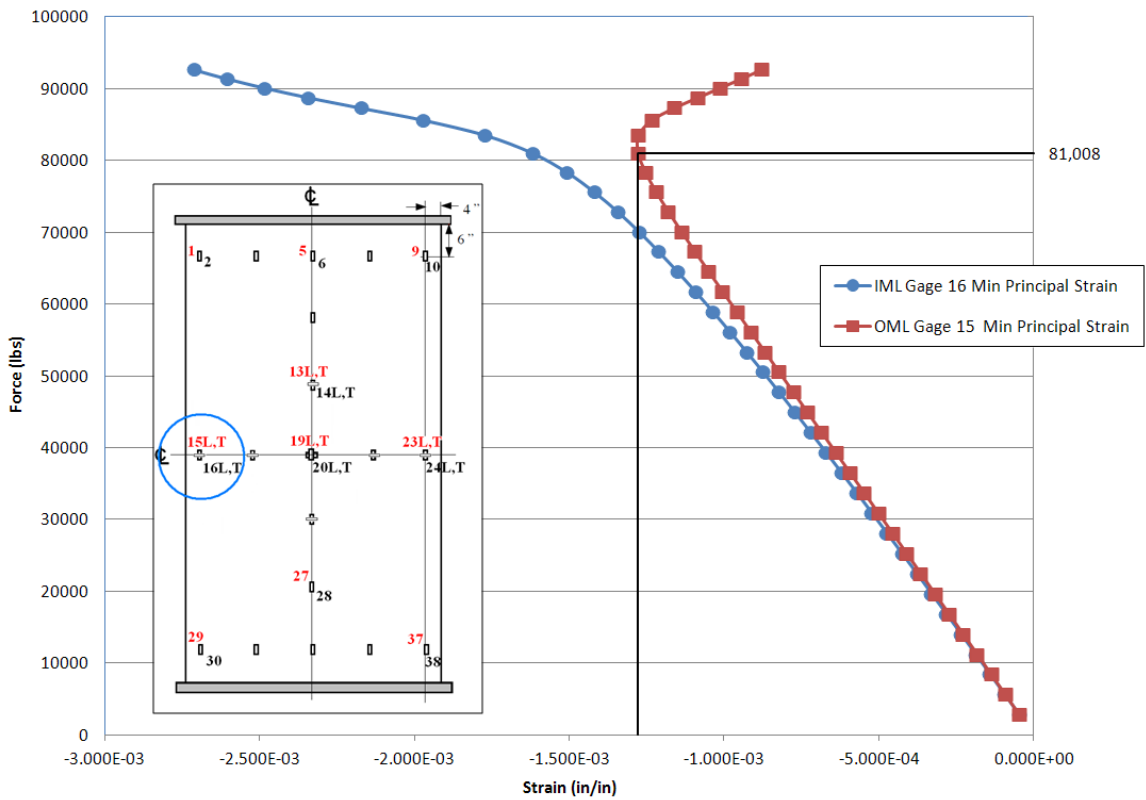


Figure 42.—Load versus minimum principal strain plots for gages 15 and 16.

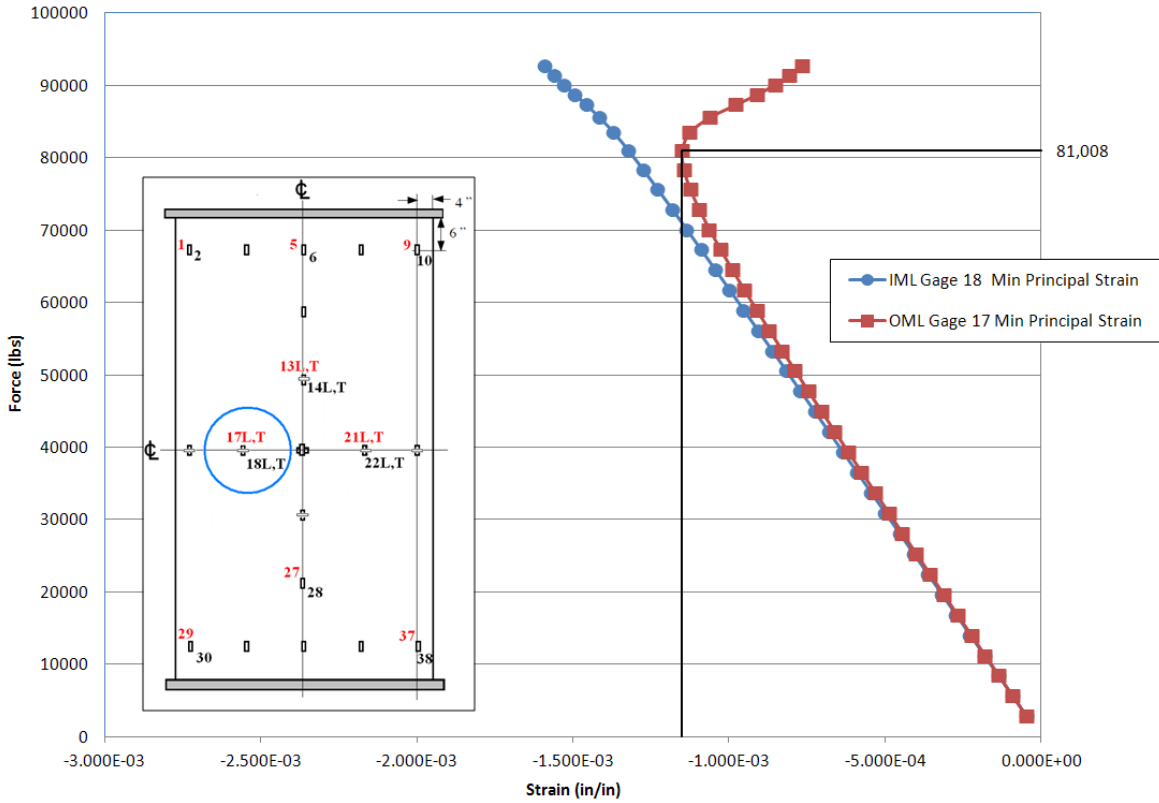


Figure 43.—Load versus minimum principal strain plots for gages 17 and 18.

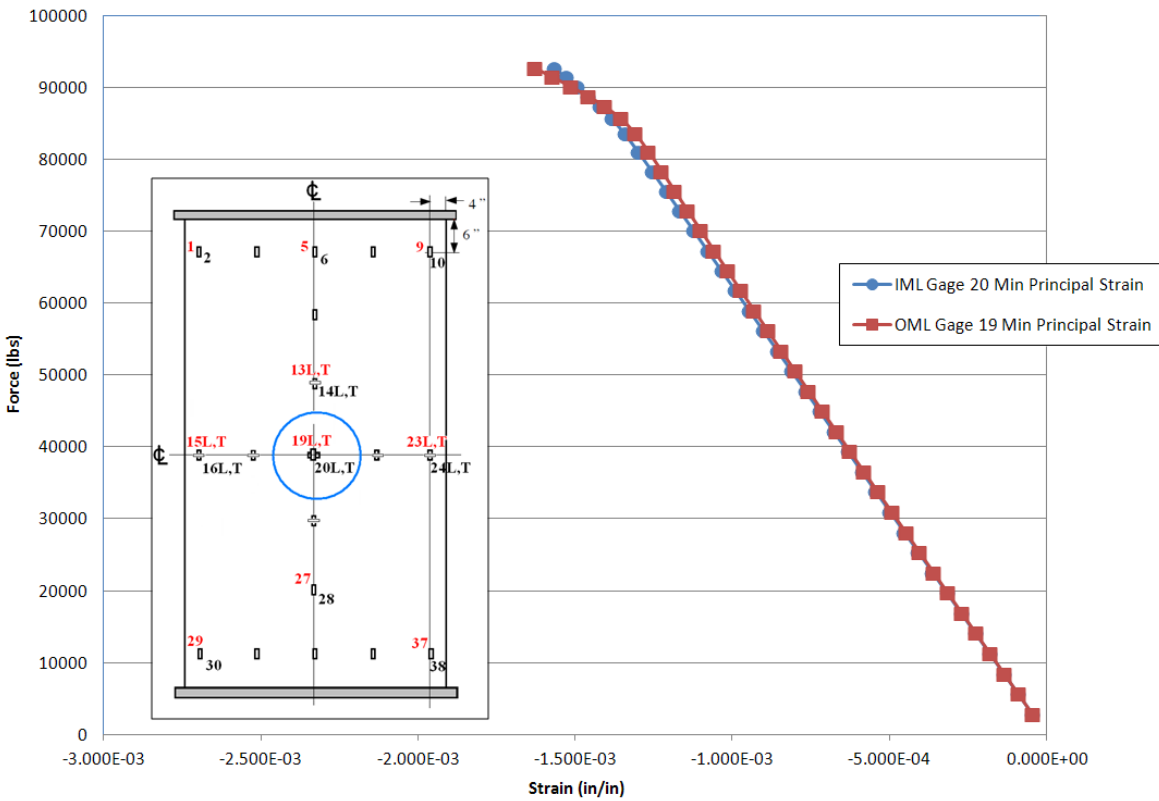


Figure 44.—Load versus minimum principal strain plots for gages 19 and 20.

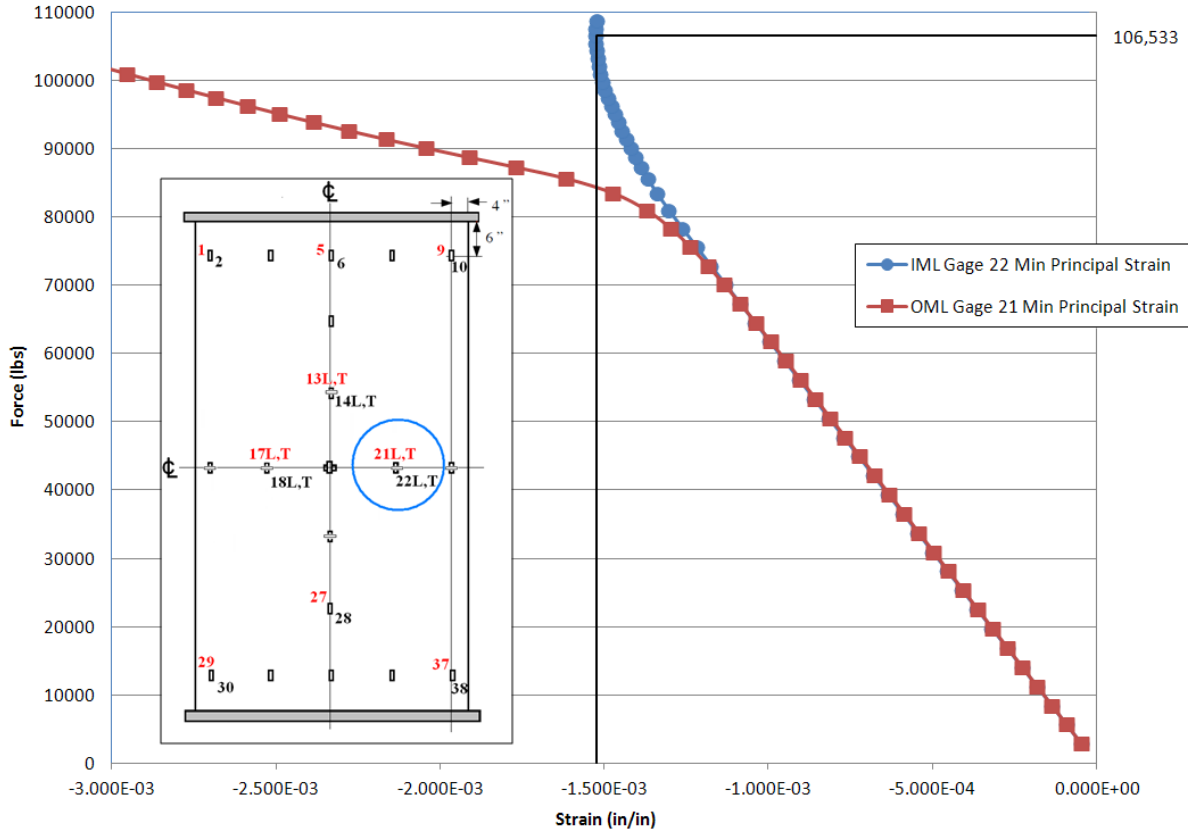


Figure 45.—Load versus minimum principal strain plots for gages 21 and 22.

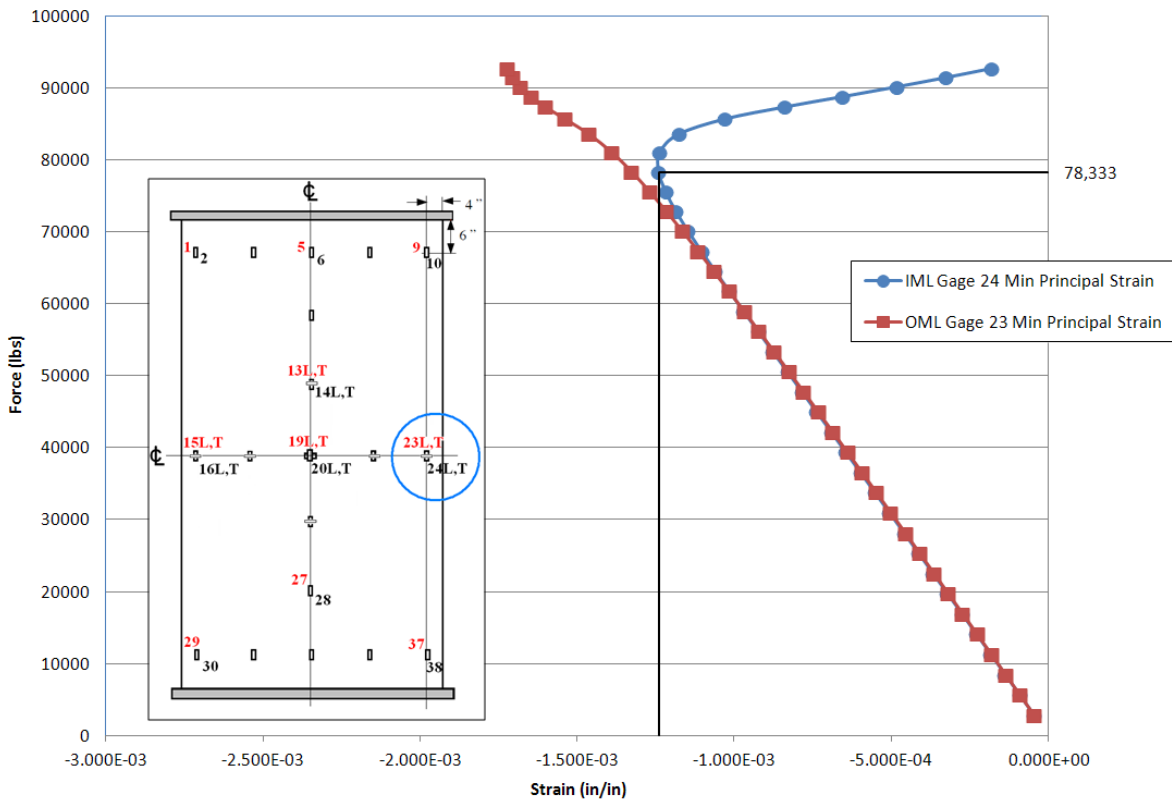


Figure 46.—Load versus minimum principal strain plots for gages 23 and 24.

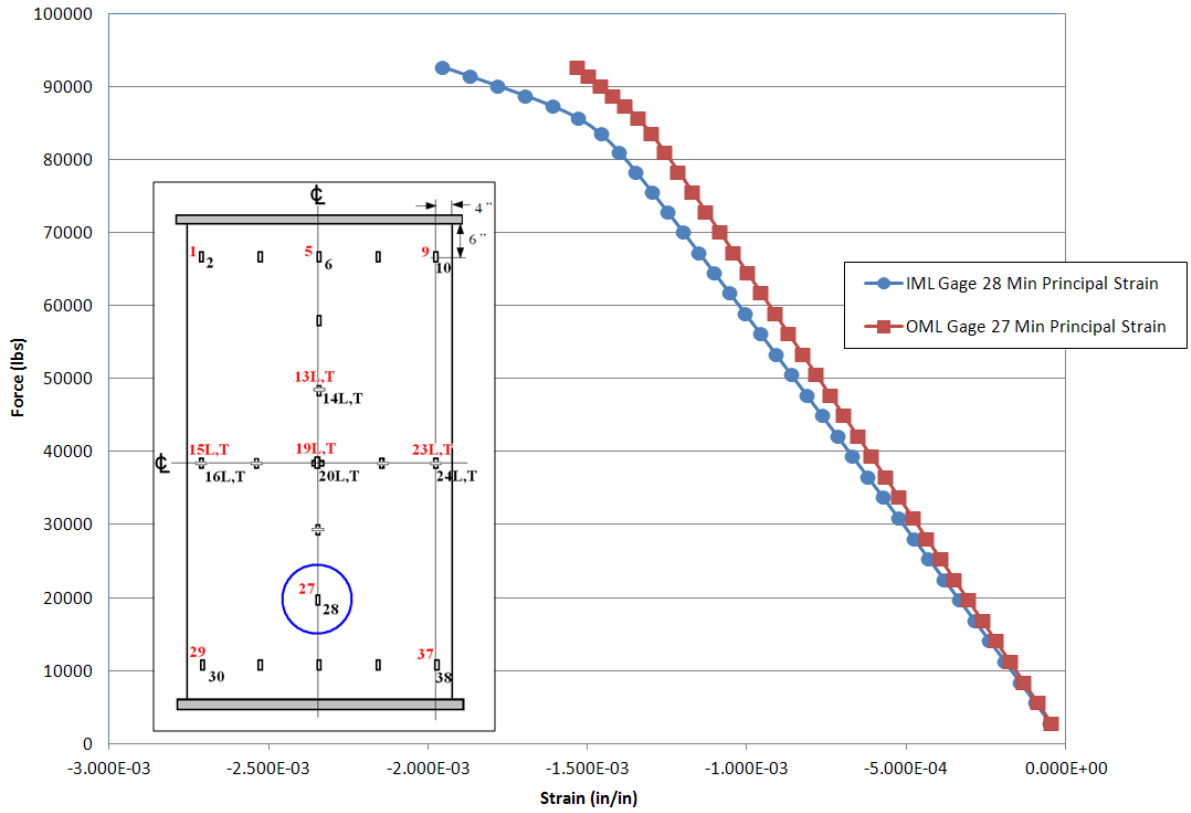


Figure 47.—Load versus minimum principal strain plots for gages 27 and 28.

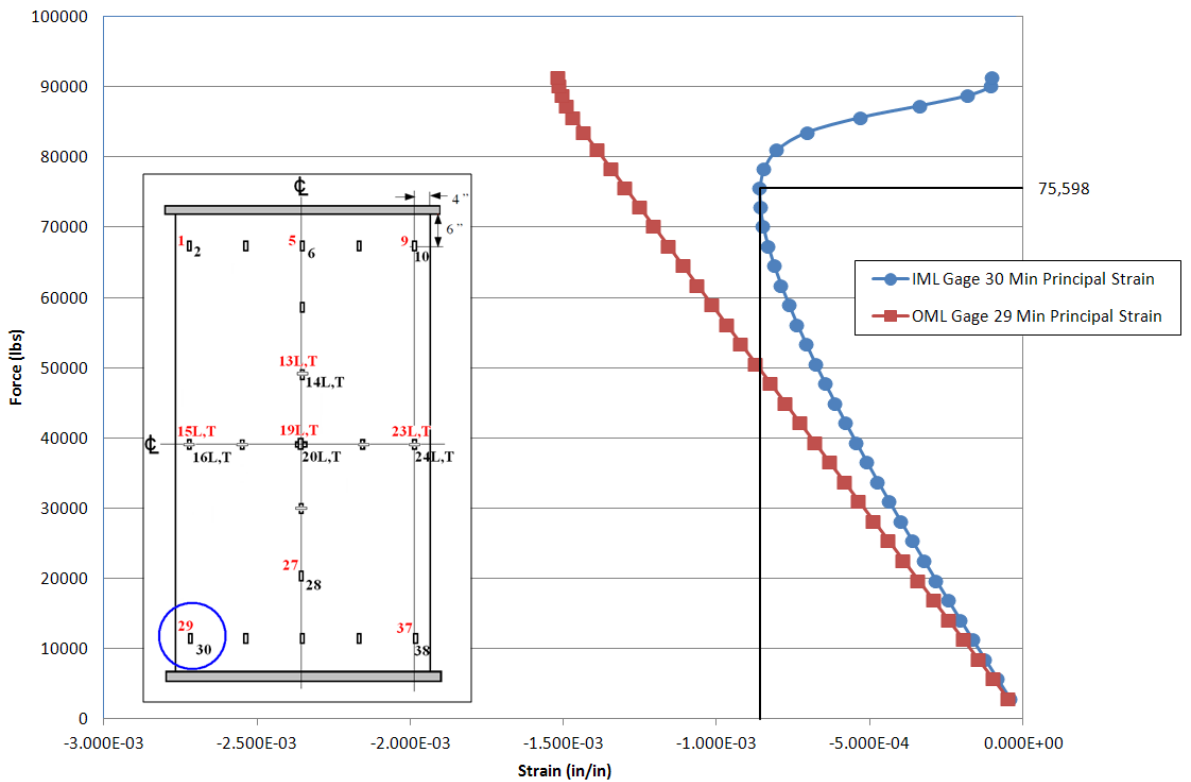


Figure 48.—Load versus minimum principal strain plots for gages 29 and 30.

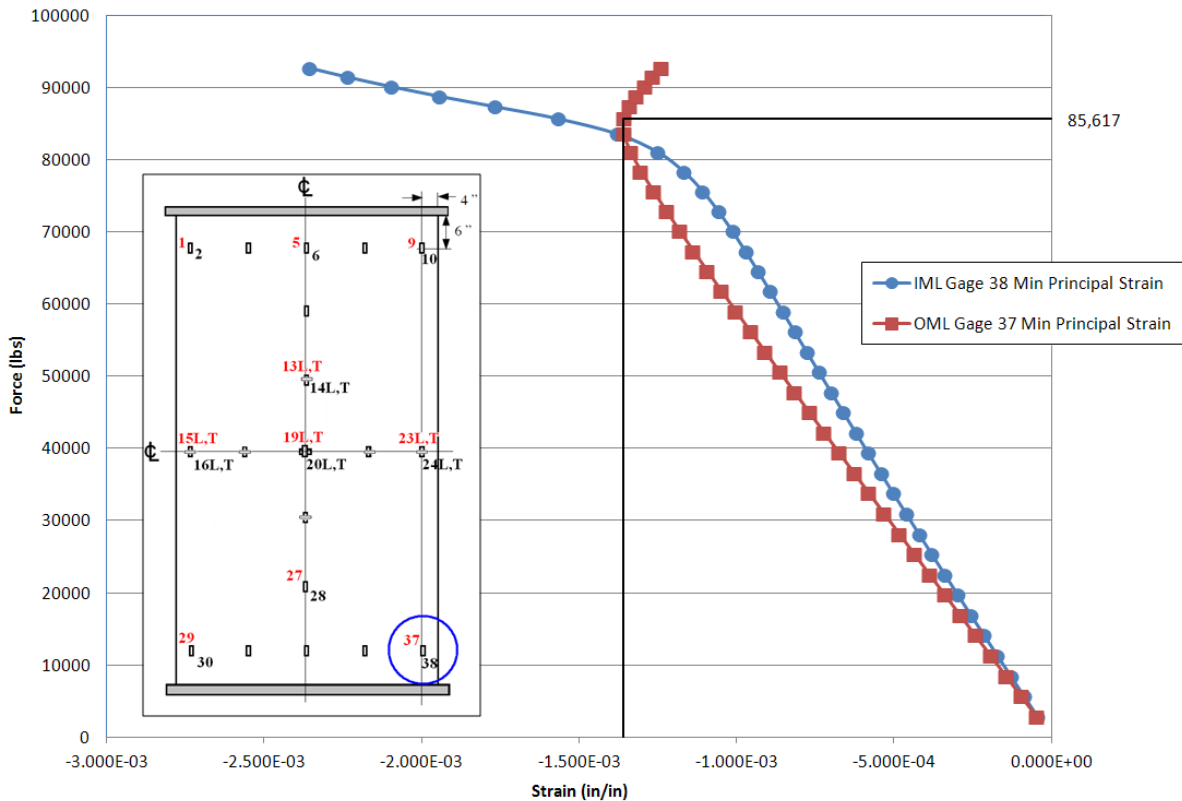


Figure 49.—Load versus minimum principal strain plots for gages 37 and 38.

Figure 50 illustrates another method to predict quantitatively the onset of panel buckling. This method uses a sudden change in panel stiffness to predict the buckling load. The panel compressive secant stiffness, P/U , is determined from the reaction load versus end-shortening data, as plotted in Figure 32. The tangent stiffness, dP/dU , is derived from the load-displacement curve. Initially, while the panel deforms linearly, the secant and tangent stiffnesses coincide. The vertical line is drawn at the point where the tangent stiffness, dP/dU , suddenly decreases and deviates from the secant stiffness curve. For the 12-by 7.67-ft honeycomb composite panel, this sudden change in the stiffness occurs at an axial compression (end-shortening) of 0.182 in. From the reaction load versus end-shortening data, this axial compression corresponds to a load of 78,332 lb. Thus, the predicted panel buckling load of 78,332 lb is a global panel prediction as opposed to local strain reversal prediction method of Singer et al. (1998). This is also in agreement with the middle left side strain gage (Figure 45, Gages 23 and 24) which shows a buckling onset load of 78,333 lb. Again, the postulated buckling load is somewhat subjective and based upon the judgment of the location where a sudden decrease in the stiffness occurs. In Figure 50, the vertical dotted line is drawn where the decrease in stiffness changes from 1.85 to 2.72 percent. Beyond the vertical dashed line, the decrease in stiffness jumps successively to 5, 11, 25, and 40 percent.

In the ANSYS solid element model, the radial (out-of-plane) displacements do not vary noticeably between the OML and IML surfaces as seen in Figure 51 and Figure 52. Examining these model displacement fields, Figure 51 and Figure 52 show the evolution of the out-of-plane or radial displacement, obtained from the numerical analysis, as the applied compressive load is increased. Both figures show that the out-of-plane (radial) displacement was negligible up to the load of 75,598 lb, which is the buckling load predicted by the axial strains at gage locations 1 and 2 and locations 29 and 30, as listed in Table 5. However, Figure 53 and Figure 54 show that the axial displacements vary significantly between the OML and IML surfaces, especially in the regions near the top and bottom test fixtures. Figure 53 and Figure 54 show the evolution of the in-plane or longitudinal displacement, obtained from the numerical analysis, as the applied compressive load is increased. The contour plot variations between

the OML axial displacements in Figure 53 and the IML axial displacements in Figure 54 explain why the slopes of the load versus strain curves for the OML and IML surfaces are so different even before the panel buckles at the top (Figure 38, Figure 39, and Figure 40) and the bottom of the panel (Figure 47, Figure 48, and Figure 49). Yet, the load versus strain curve along the midplane (Figure 42 to Figure 46) for the OML and IML are the same until the buckling load, because the midplane axial displacements (Figure 53 and Figure 54) remain the same until the point of buckling at 75,598 lb.

For the OML surface, Figure 55 shows that the minimum principal strain (compressive) was minimal up until the point of buckling at 75,598 lb as seen in the out-of-plane (radial) displacements in Figure 51. Similarly, Figure 56 shows that the minimum principal strain (compressive) on the IML surface was minimal up until the same point of buckling which is also seen in the out-of-plane (radial) displacements in Figure 52. Both strain contour plots display asymmetry which was due to the scaled asymmetric geometric imperfections superimposed from the linear buckling modes.

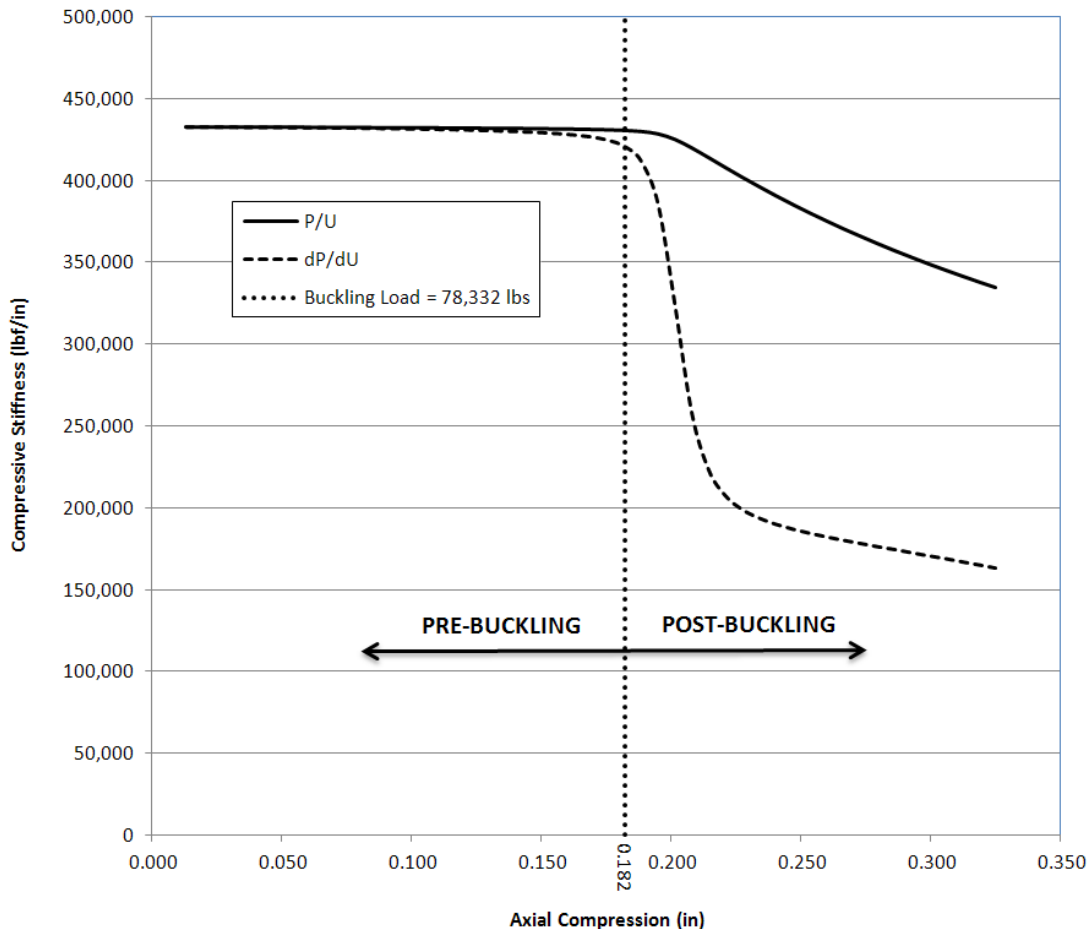


Figure 50.—Stiffness versus axial compression for the ANSYS Solid FEM of the 12- by 7.67-ft honeycomb sandwich panel

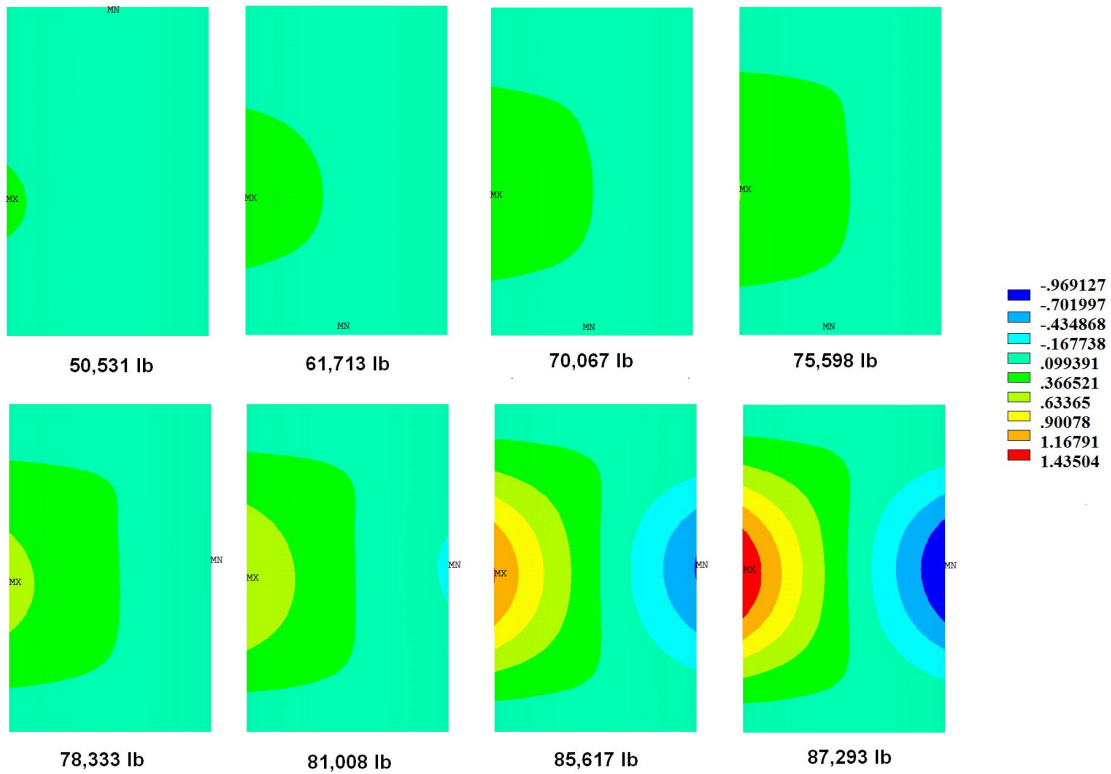


Figure 51.—ANSYS Solid FEM, OML radial (x-axis or out-of-plane) displacement contour plots versus load.

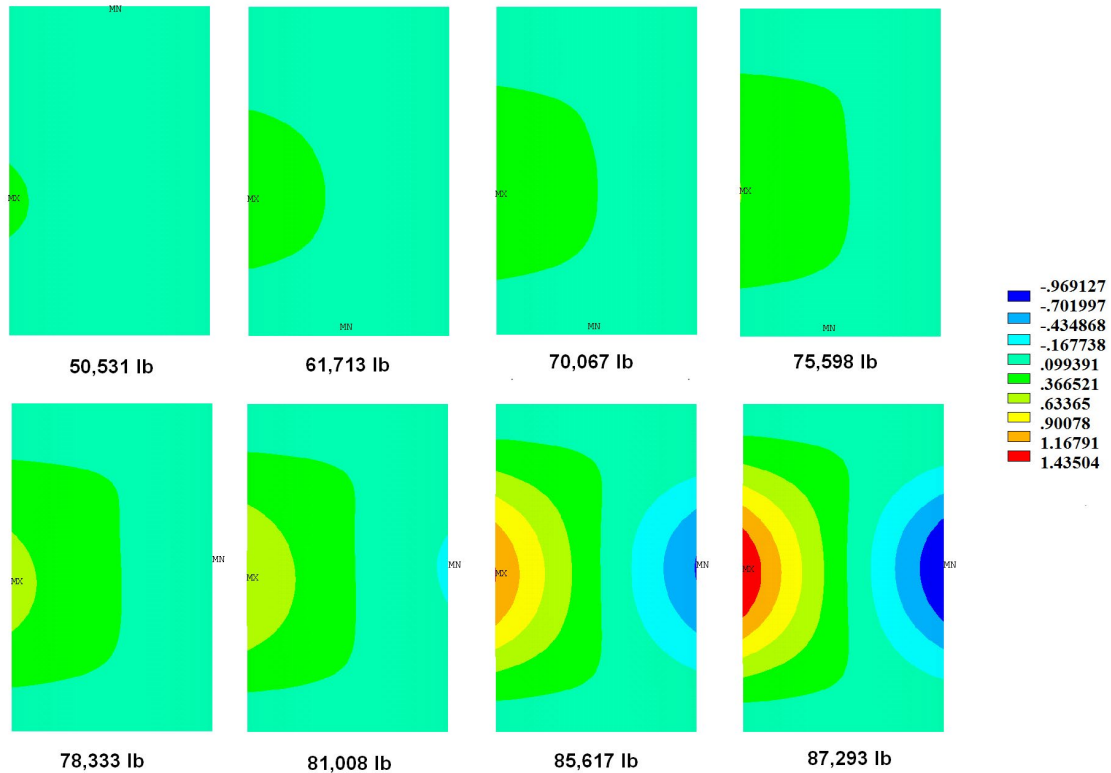


Figure 52.—ANSYS Solid FEM, IML radial (x-axis, or out-of-plane) displacement contour plots versus load.

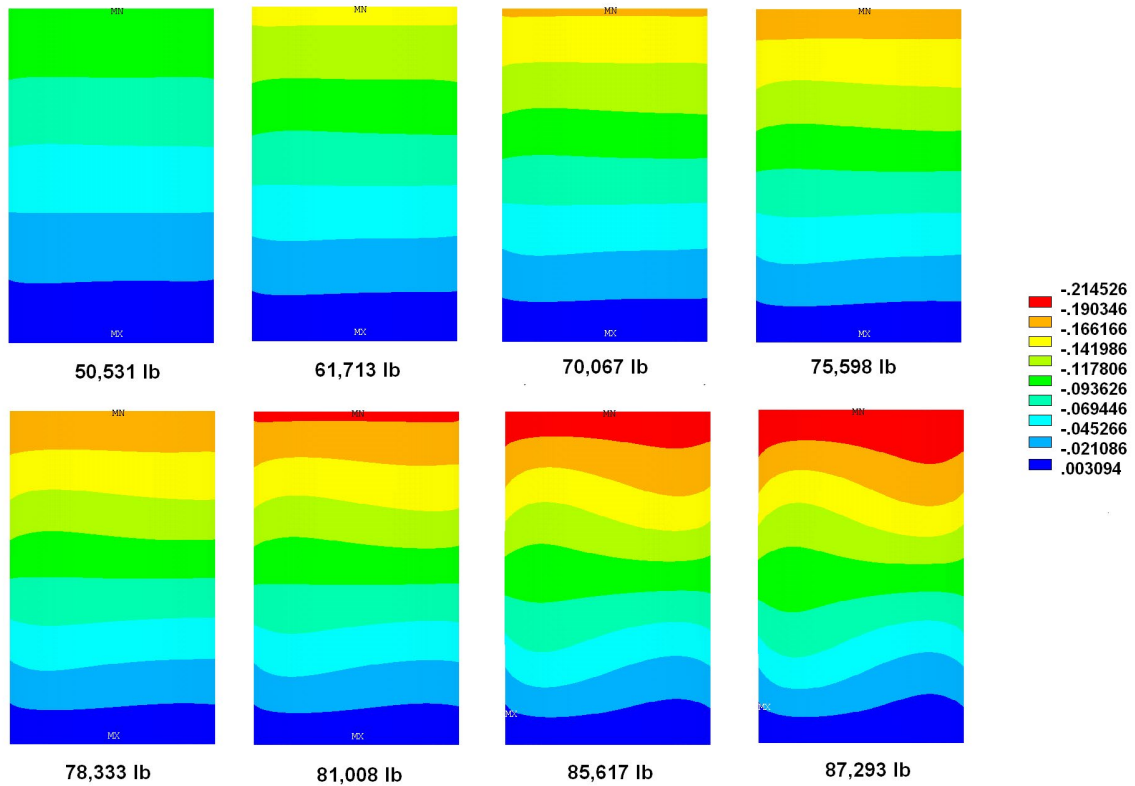


Figure 53.—ANSYS Solid FEM, OML axial (z-axis or longitudinal) displacement contour plots versus load.

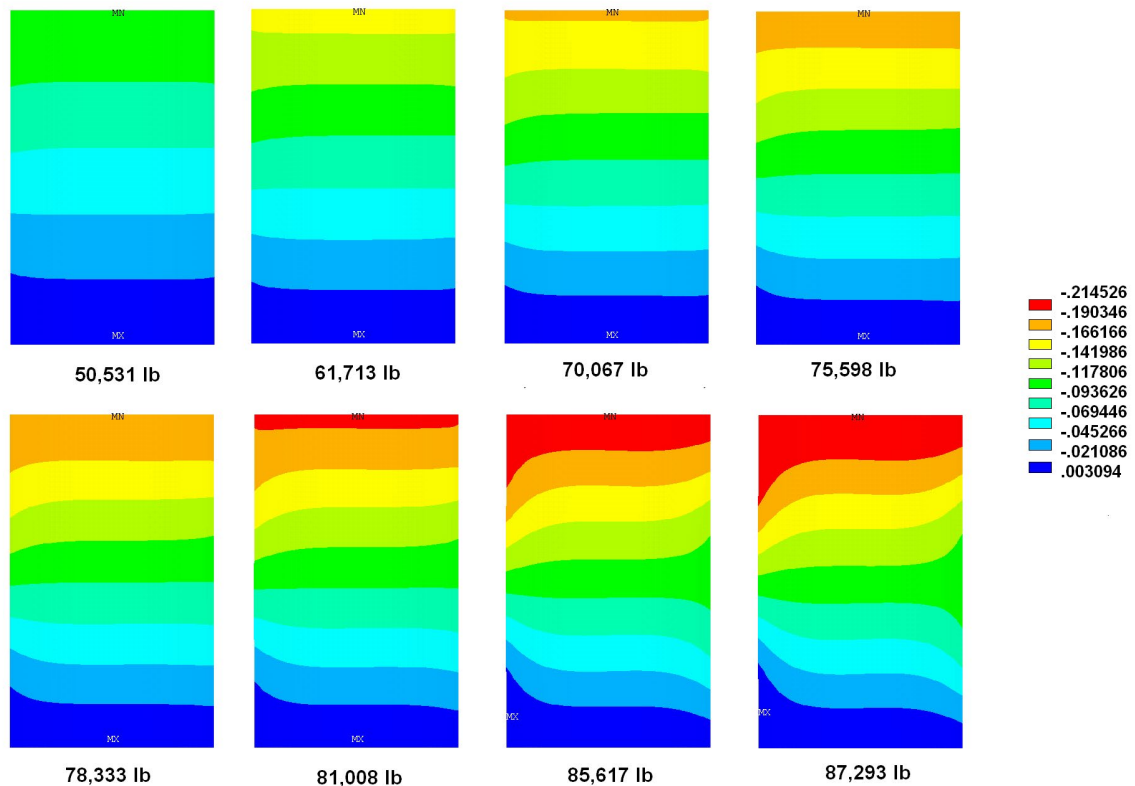


Figure 54.—ANSYS Solid FEM, IML axial (z-axis or longitudinal) displacement contour plots versus load.

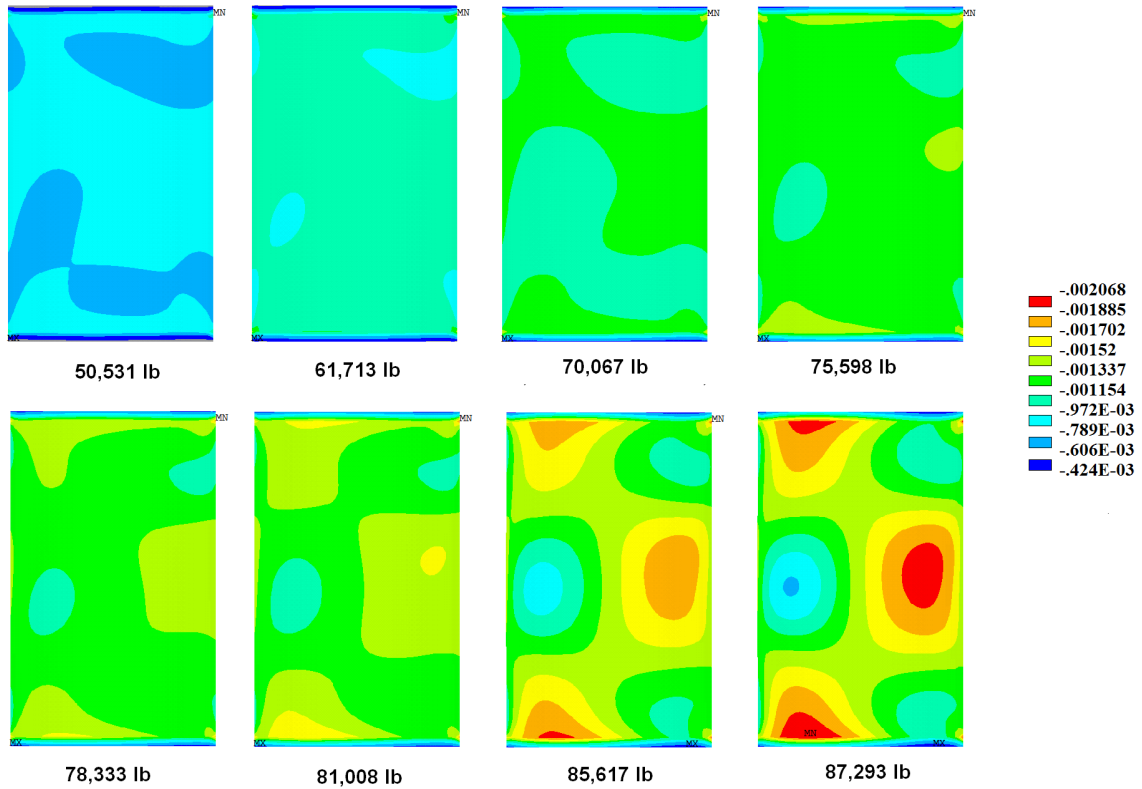


Figure 55.—ANSYS Solid FEM, OML minimum principal strain (z-axis or longitudinal).

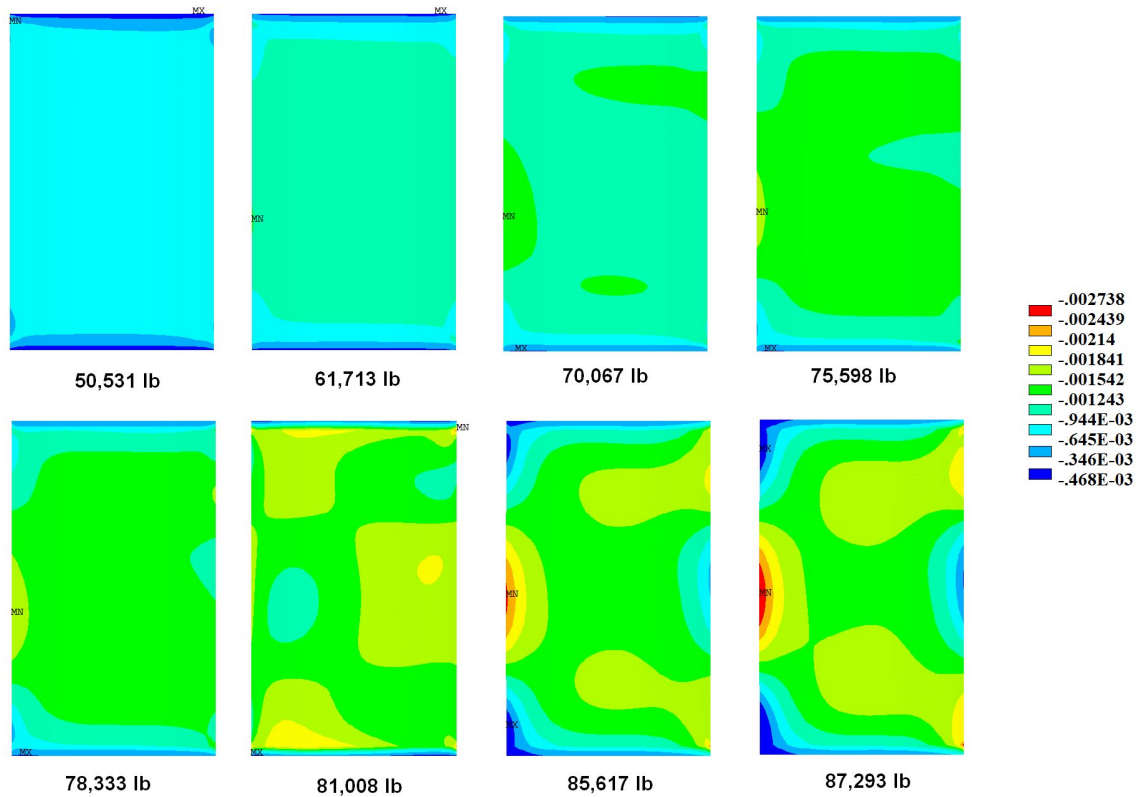


Figure 56.—ANSYS Solid FEM, IML minimum principal strain (z-axis or longitudinal).

5.0 FRF Sandwich Panel Nonlinear Buckling Analysis

A 1/6th FRF sandwich panel was constructed according to the design shown in Figure 8. Based on the linear eigenvalue buckling analyses presented in Section 3.0, a buckling test article size of 12- by 7.67-ft was selected. This panel size maintains the full 1/6th panel aspect ratio and is also within the “sweet spot” identified in Figure 15. Measurements of the actual 1/6th FRF sandwich panel revealed some variance of the panel cross-section dimensions from the design shown in Figure 8. In particular, the average height of the panel was 0.94 in. (versus 1-in. in the design), the internal webs were 0.042 in. thick and spaced at 2.54-in. (versus 0.04- and 2.5-in. in the design), and the facesheet plus the winding layer thickness was 0.056-in. (versus 0.068 in. in the design). New properties for the FRF panel were generated based on these actual dimensions, with exception of the facesheet plus winding layer thickness. This thickness variation is due to the presence of a different amount of matrix material than expected during the infiltration, bagging, and curing process, whereas the amount of fiber material is known and fixed. It would thus be incorrect to increase the thickness of the facesheet without also decreasing its fiber volume fraction, which would necessitate changing all of the facesheet mechanical properties. Instead, the original design facesheet thickness of 0.048 in. was maintained, as this will provide close to the proper contribution of the facesheet to the panel stiffness.

The updated panel effective stiffness matrices, again referred to a reference plane at the midpoint of the top facesheet, are,

$$\mathbf{A} = \begin{bmatrix} 948 & 373 & 0 \\ 373 & 937 & 0 \\ 0 & 0 & 391 \end{bmatrix} \times 10^3 \text{ lb/in} \quad \mathbf{B} = \begin{bmatrix} 423 & 166 & 0 \\ 166 & 418 & 0 \\ 0 & 0 & 174 \end{bmatrix} \times 10^3 \text{ in} - \text{lb/in} \quad \mathbf{D} = \begin{bmatrix} 372 & 145 & 0.5 \\ 145 & 369 & 0.5 \\ 0.5 & 0.5 & 152 \end{bmatrix} \times 10^3 \text{ in}^2 - \text{lb/in}$$

While the extensional (**A**) and coupling (**B**) stiffness matrices have changed slightly, a significant change in the bending stiffness (**D**) has occurred, mainly because of the 6 percent reduction in the overall panel thickness compared to the design.

The Abaqus nonlinear buckling analysis results for the 12- by 7.67-ft FRF sandwich panel model are shown in Figure 57. Note that a fixed increment size was used for these analyses. Cases in which the first ten linear eigenvalue buckling modes were used to seed the model were analyzed with scale factors of both 0.015 in. and 0.02 in. In addition, a case with a scale factor of 0.02 in., but only seeded with the first linear eigenvalue buckling mode was analyzed. All three of these cases gave nearly identical load-displacement results, characterized by the onset of nonlinearity at a load of 92,400 lb. This compares well with the first linear buckling eigenvalue for the panel of 95,900 lb (3.8 percent difference). Also shown in Figure 57 is the buckling mode associated with the three nearly coincident seeded nonlinear cases and the first mode associated with the linear eigenvalue buckling analysis. These modes are the same, and they correspond to the circumferential buckling mode C from Figure 15.

Figure 57 also includes Abaqus nonlinear buckling results for the same FRF panel with no imperfection, using the same increment size that was sufficient for the cases seeded with imperfection. Clearly, it appears that the case with no imperfection is giving a completely different buckling prediction. The panel response remains linear up to a load of 133,700 lb (a difference of 45 percent from the seeded cases) and takes a different buckling mode, similar to the axial or column buckling mode A in Figure 15. However, close examination of the Abaqus output for this case reveals that, once the load associated with the linear eigenvalue of the panel was exceeded, Abaqus was reporting negative eigenvalues. The increments associated with these negative eigenvalues are indicated in Figure 57. Negative eigenvalues, in a linear regime such as this, are an indication of numerical problems in the finite element code, and the associated results are thus unreliable. Note that, although not shown herein, decreasing the load increment size did not affect these results.

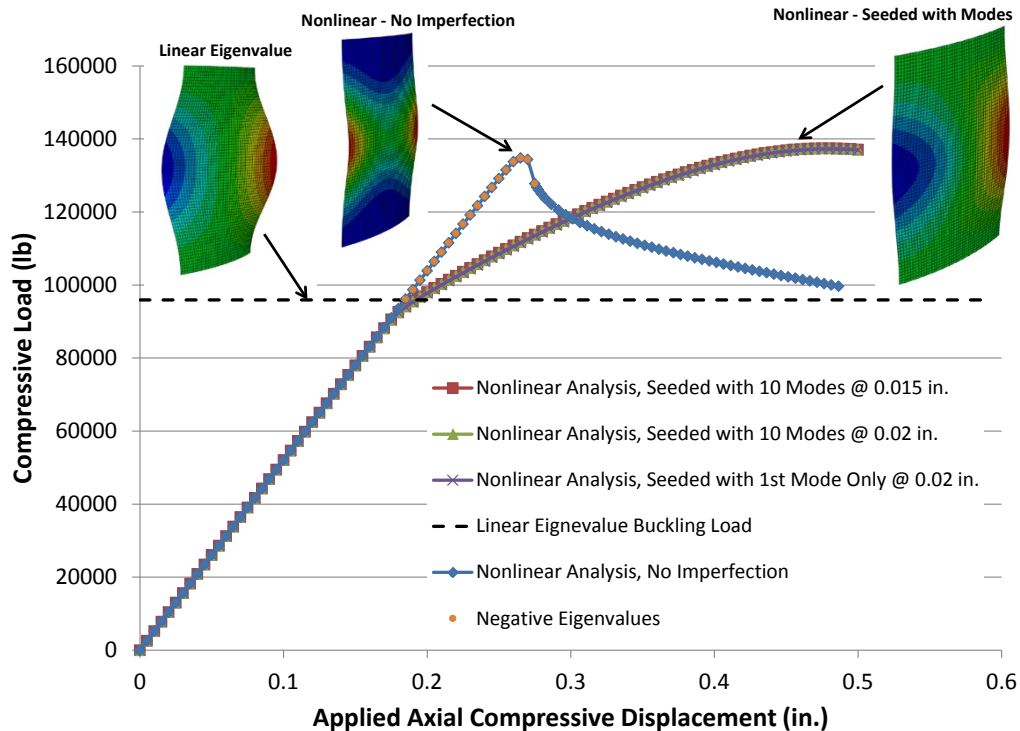


Figure 57.—Abaqus nonlinear buckling analyses of a 12- by 7.67-ft FRF sandwich panel.

The actual 1/6th FRF panel was cut to produce a 12- by 7.67-ft buckling test article. This test article was scanned to measure its geometric imperfection. Measurements of the deviation of the panel from cylindrical, normal to the panel surface, were taken along the 12-ft length of the panel close to the left edge, close to the right edge, and along the center. The results are shown in Figure 58. The panel takes a slight saddle shape, with the most severe imperfection measured along the left edge with an approximated maximum magnitude of 0.02 in.

To assess the impact of the imperfection on the FRF panel predicted buckling response, the measured left edge imperfection was considered. First, the measured curve, which ends at 133 in., was extended to the full panel length of 144 in. by scaling all axial point locations by $144/133 = 1.083$. Then a three point central moving average was taken to filter the data, and a few outlier points were removed, resulting in the approximation of the imperfection shown in Figure 59. This approximation was then used as spline points in Abaqus to generate the geometry of the long edge of the panel and subsequently swept along the panel θ -direction to generate the full panel shell geometry. This procedure does not capture any variation of the imperfection in the θ -direction, but has been shown by Myers et al. (2013) to provide a good approximation of cylindrical panel imperfection for buckling analyses.

Nonlinear buckling analysis results for the 12- by 7.67-ft FRF sandwich panel, including the left imperfection (bow), are shown in Figure 60. The prediction that includes the geometric imperfection matches very closely with the nonlinear analysis with no imperfection, but is also similarly plagued by the negative eigenvalues, which indicate an unreliable result. The predicted column buckling mode also matches the no imperfection case.

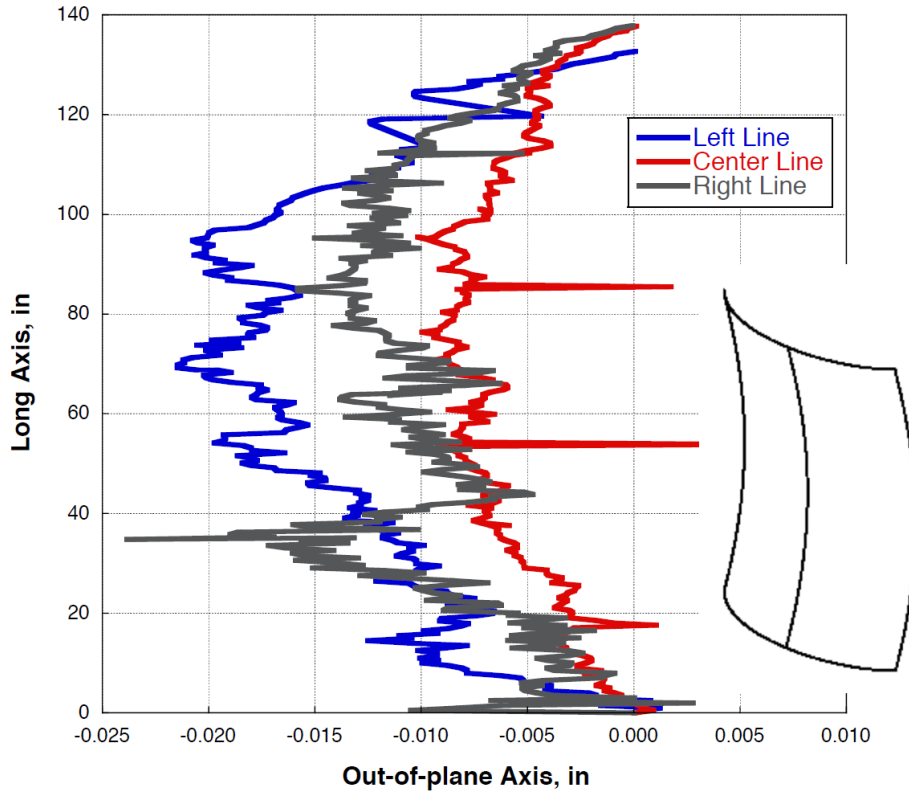


Figure 58.—Measured geometric imperfections in the FRF 12- by 7.67-ft buckling test article.

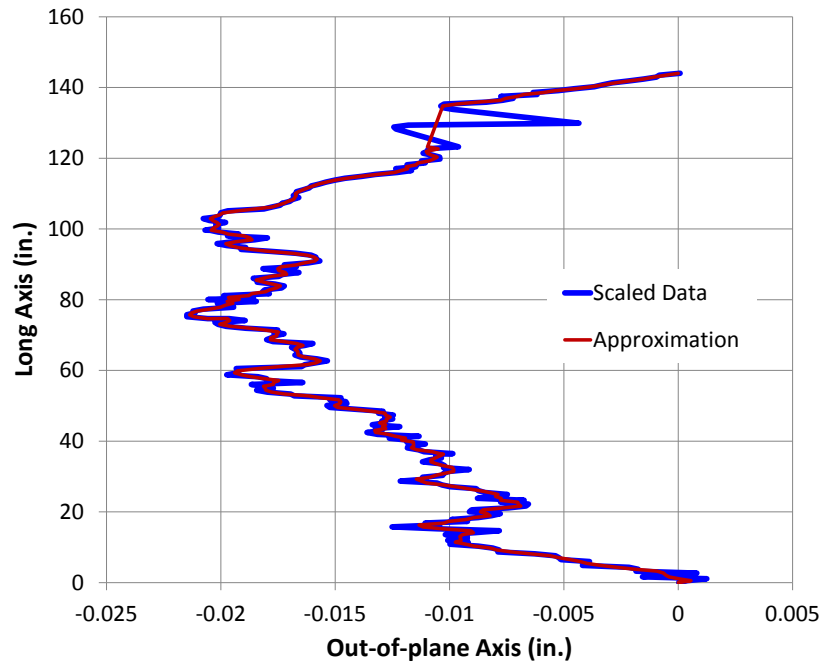


Figure 59.—Measured and approximated left edge geometric imperfection in the FRF 12- by 7.67-ft buckling test article.

To overcome the unreliable predictions, the Riks arc-length method, available within Abaqus, was used, in combination with a very small loading increment. It should be noted that, using the Riks method without limiting Abaqus to a very small loading increment resulted in prediction similar to those shown in Figure 60 with negative eigenvalues, which indicate a numerical problem in the solution. Forcing Abaqus to use a very small loading increment without using the Riks method resulted in divergence near the load associated with the first linear eigenvalue. In this case, Abaqus is unable to reach a converged solution at a given time increment, and the code execution stops. As shown in Figure 61, using the Riks method in combination with a very small loading increment resulted in both the case with no imperfection and the case with the left edge bow shape matching the case seeded with the first ten linear eigenvalue buckling modes very closely. The circumferential buckling modes also matched that of the seeded cases. All three of these cases predict the onset of buckling, evident as a knee in the load versus deflection curves, at a load level very close to the linear eigenvalue buckling load of 95,900 lb.

It should be noted that previous work by Myers et al. (2013) indicated that qualitatively similar imperfections with magnitudes on the order of that shown in Figure 58 did have a sizable impact on the buckling response of cylindrical arc-segment honeycomb sandwich panels. However, the 1/16th panels considered in that study were a different size than the FRF panel considered herein (5- by 3-ft versus 12- by 7.67-ft), and they buckled in a different mode. These differences are likely to account for the fact that, in present investigation, the imperfections were observed to have little effect on the Riks buckling analysis.

Figure 62 shows axial strain field and the radial displacement field predicted by the Riks method with the very small loading increment just after the buckling knee at an applied axial displacement of -0.19 in. Note that, because this shell-based model used homogenized effective stiffness terms to define the material (rather than ply definitions) the predicted strain fields are constant through the panel thickness. Note the similarity of Figure 62(a) (FRF panel) to Figure 55 (honeycomb sandwich panel) and the similarity of Figure 62(b) (FRF panel) to Figure 51 (honeycomb sandwich panel). The FRF and honeycomb sandwich plots are mirrored with respect to each other because, as can be seen from comparing Figure 62(b) to Figure 51, opposite edges were predicted to buckle outwards in the simulations.

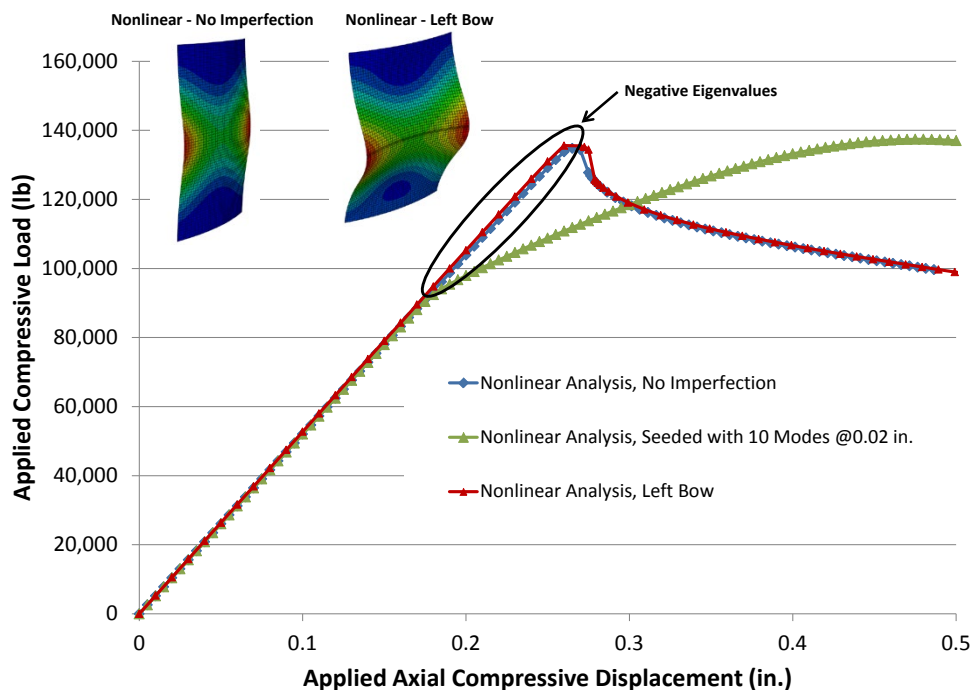


Figure 60.—Abaqus nonlinear buckling analyses of a 12- by 7.67-ft FRF sandwich panel.

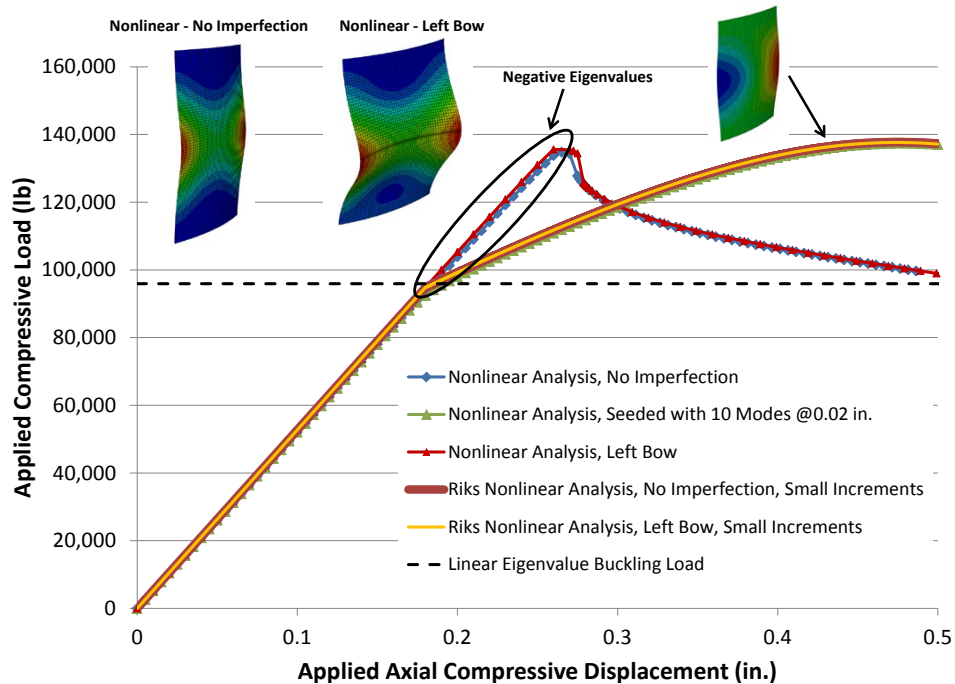


Figure 61.—Abaqus nonlinear buckling with Riks analyses of a 12- by 7.67-ft FRF sandwich panel.

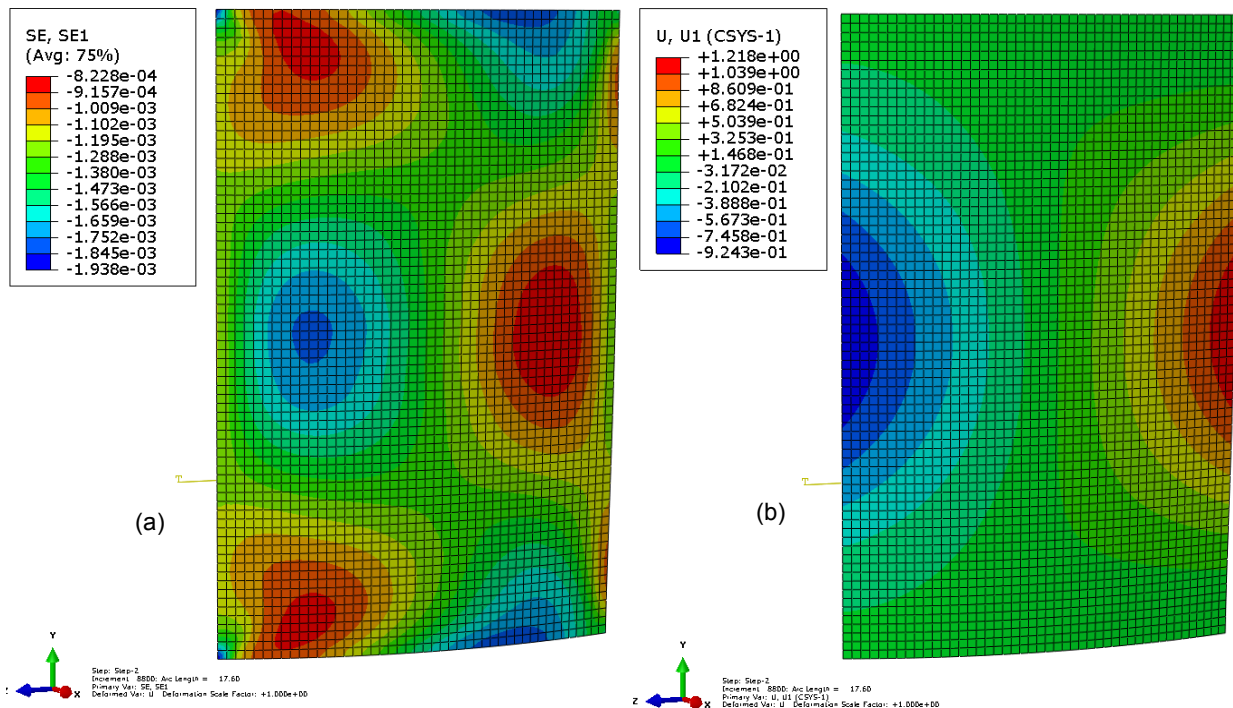


Figure 62.—Fields predicted by the Abaqus nonlinear buckling analyses of a 12- by 7.67-ft FRF sandwich panel at an applied global displacement of -0.19 in., (a) axial strain field, and (b) radial displacement field.

6.0 Conclusions

This report presents finite element based buckling analyses for 1/6th arc-segment panel of a full 33-ft diameter cylindrical barrel section of a payload fairing structure. Both linear and nonlinear analyses, shell and solid models, and honeycomb sandwich and fiber reinforced foam (FRF) sandwich configurations were considered using the ANSYS and Abaqus commercial finite element codes. The panel cross sections geometries considered were chosen to be representative of realistic Space Launch Systems (SLS) fairing barrel panels. Linear eigenvalue shell element based buckling analyses indicated that a smaller 12- by 7.67-ft panel, four of which could be cut from the full 27- by 17.25-ft panel 1/6th arc-segment panel, could serve as a manageable compression test article, while also providing two key features in its expected buckling response. First, the initial predicted buckling mode shape was characterized by waves with alternating radial directions on the panel sides. This is representative of a classical periodic full cylinder buckling mode, where waves with alternating radial direction progress circumferentially around the cylinder. Second, there was a large (approximately 50 percent) difference between the first and next lowest predicted buckling eigenvalue. A large spread between eigenvalues is desirable in terms of test versus prediction correlation because potential imperfections in the panel construction and the test set up are then less likely to cause a different actual buckling mode. Based on these results, the 12- by 7.67-ft panel dimensions were recommended for large buckling test panels for both the honeycomb sandwich and FRF sandwich panel concepts. The shell-based linear buckling analyses performed using ANSYS and Abaqus were in very good agreement, while, qualitatively, the honeycomb and FRF sandwich configurations performed quite similarly. Of course, some quantitative difference was present due to the slightly lower effective stiffness and different dimensions of the two configurations.

Shell-based nonlinear buckling analyses of various honeycomb sandwich panel sizes showed that, once again, the buckling predictions of ANSYS and Abaqus were in very good agreement. In these cases, the first ten linear eigenvalues were used to seed the nonlinear analyses with geometric imperfection in both codes. Then, using ANSYS, a detailed nonlinear buckling analysis study was performed with a solid element model of the previously determined smaller 12- by 7.67-ft panel. First, this model was used to show good agreement with the ANSYS shell element based nonlinear model in terms of mode and buckling load. Then, detailed strain histories were examined at various locations over the panel area that represent potential strain gage locations for a test panel. By monitoring the strain histories on the front and back sides of the panel at a given location, it was shown that the point of a strain reversal could be used as an estimate of the onset of buckling.

Finally, shell element based nonlinear buckling analyses of the 12- by 7.67-ft FRF panel were performed using Abaqus. It was shown that, as in the case of the honeycomb sandwich configuration, when seeded with the first ten linear buckling modes, the FRF panel nonlinear predictions matched the mode and buckling load predicted by linear analysis closely. Further, the predicted load versus displacement curve was qualitatively similar to that of the honeycomb sandwich. However, with no imperfection, Abaqus predicted a different axial (column-like) buckling mode with much higher buckling load. These results were characterized by negative eigenvalues while the panel remained in a linear regime, an indication of unreliable results. Similar unreliable results were obtained when including geometric imperfections, measured from an actual manufactured 12- by 7.67-ft FRF test panel, in the analysis. To overcome these issues in the nonlinear analysis, a Riks arc-length method analysis, wherein a very small loading increment size was enforced, was performed for the FRF panel with the realistic imperfections in Abaqus. These results matched the prediction for the FRF panel seeded with the first ten linear buckling modes and are expected to be a good prediction of the performance of the actual FRF test panel.

7.0 References

Aboudi, J., Arnold, S.M., and Bednarczyk, B.A. (2013) *Micromechanics of Composite Materials: A Generalized Multiscale Analysis Approach*, Elsevier, Oxford, UK.

- Bednarczyk, B.A. and Arnold, S.M. (2002) "MAC/GMC 4.0 User's Manual Volume 2: Keywords Manual" NASA/TM—2002-212077/VOL2.
- Bednarczyk, B.A., Yarrington, P.W., Lucking, R.C., Collier, C.S., and Ainsworth, J.J. (2011) "Efficient Design and Analysis of Lightweight Reinforced Core Sandwich and PRSEUS Structures" NASA/TM—2011-217198.
- Bednarczyk, B.A., Arnold, S.M., and Hopkins, D.A. (2010) "Design of Fiber Reinforced Foam Sandwich Panels for Large Ares V Structural Applications" NASA/TM—2010-216823.
- Evonik Industries (2013) Rohacell HF Product Information, <http://www.rohacell.com/sites/dc/Downloadcenter/Evonik/Product/ROHACELL/product-information/ROHACELL%20HF%20Product%20Information.pdf>. Accessed September 19, 2013.
- Hexcel Corp. (2013) HexWeb CR III Product Data, http://www.hexcel.com/Resources/DataSheets/Honeycomb-Data-Sheets/CR3_us.pdf. Accessed September 6, 2013.
- Hong, C. S., Jun S. M. (1989) "Buckling behavior of laminated composite cylindrical panel with initial imperfections," Winter Annual Meeting of the American Society of Mechanical Engineers, co-sponsored by Pressure Vessels and Piping Division & Aerospace Division, ASME, San Francisco, CA, Dec. 10-15, PVP-Vol. 183, AD-Vol. 18.
- HyperSizer Structural Sizing Software (2013), Collier Research Corp., Newport News, VA, www.HyperSizer.com. Accessed September 6, 2013.
- Jones, R. M. (1999) *Mechanics of Composite Materials, 2nd Edition*, Taylor & Francis, Inc., Philadelphia, PA.
- Lockheed Martin (2010) *Orion Materials and Design Allowables*, Rev. D, 22 Sept.
- Myers, D.E., Pineda, E.J., Zalewski, B.F., Kosareo, D.N., and Kellas, S. (2013) "Buckling Testing and Analysis of Honeycomb Sandwich Panel Arc Segments of Full-Scale Fairing Barrel – Part 1: 8-ply In-Autoclave Facesheets," NASA/TM—2013-217822/PART1.
- Singer, J., Arbocz, J., T. Weller (1998) *Buckling Experimental Methods in Buckling Thin Walled Structures, Basic Concepts, Columns, Beams and Plates – Volume 1*, John Wiley & Sons, Inc., New York.
- Sleight, D.W., Sreekantamurthy, T., Kosareo, D.N., Martin, R.A., and Johnson, T.F. (2011) "Structural Design of Ares V Interstage Composite Structure," 52nd AIAA/ASME/ASCE/AHS/ ASC Structures, Structural Dynamics and Material Conference, Denver, Colorado, 4-7 April, AIAA 2011-1790.
- Unisorb Installation Technologies (5/2010), UNISORB Grouting Products - Application & Specification Guidelines, <http://www.unisorb.com/pdf/grout%20catalog.pdf>. Accessed September 6, 2013.
- VectorPly Corp. (2013), VectorPly C-QZ 1800 Datasheet, <http://www.vectorply.com/pdf/c-qx%201800.pdf>. Accessed September 6, 2013.
- Vinson, J. R. (1999) *The Behavior of Sandwich Structures of Isotropic and Composite Materials*, Technomic Publishing Co., Lancaster, PA.
- Zalewski, B.F. and Bednarczyk, B.A. (2010) "ACT Payload Shroud Structural Concept Analysis and Optimization" NASA/TM—2010-216942.

